Accepted manuscript doi:
10.1680/jtran.23.00066

Submitted: 20 June 2023

Published online in 'accepted manuscript' format: 14 November 2024

Manuscript title: A hybrid ANN-GA back-analysis technique for local anomaly detection in railway track substructure

Authors: Shadi Fathi[1], Moura Mehravar[2] and Mujib Rahman[3]

Affiliations: [1]Department of Civil Engineering, Coventry University,United Kingdom, [2]School of Engineering, Department of Civil Engineering, University of Birmingham, United Kingdom, [3]Department of Civil Engineering, Aston University, Birmingham, Aston St. B4 7ET, United Kingdom

Corresponding author: Moura Mehravar, School of Engineering, Department of Civil Engineering, University of Birmingham, United Kingdom

E-mail: m.mehravar@bham.ac.uk

Accepted manuscript doi:
10.1680/jtran.23.00066

Abstract

The UK's ageing railway transportation network is increasingly at risk of substructure failure, often caused by malfunctioning buried drainage systems. These drainage issues lead to localised soil weaknesses in the substructure layers, which, if undetected, can result in costly maintenance interventions or, worse, catastrophic system failure. Regular non-destructive testing (NDT) assessments are essential for monitoring the condition of the substructure, yet current interpretation techniques for NDT data provide limited insight into the size, location, and even presence of weakened zones. This results in an incomplete understanding of the substructure's condition, impeding effective maintenance planning. This study proposes a novel hybrid back-analysis technique to detect weakened zones in railway substructures caused by drainage malfunctions, addressing a critical gap in existing solutions. The method employs an artificial neural network (ANN) surrogate model, trained on virtual experimental data generated through finite element (FE) simulations, and couples it with a genetic algorithm (GA) to optimise the match between modelled and measured deflections. This novel method is computationally efficient, independent of seed modulus values, and thoroughly validated for accuracy. It delivers a precise understanding of soil weaknesses in railway substructures, transforming maintenance strategies by improving safety, reducing costs, and promoting infrastructure sustainability.

Keywords: geotechnical engineering, railway substructure, soil, back-analysis technique, ground failure, drainage malfunction, condition assessment, UN SDG 9, UN SDG 11.

Introduction

The railway track infrastructure in the UK was mainly built during the 19th century, making it one of the oldest railway systems worldwide (Gunn et al., 2018). The recent increase in rail network usage and axle loads have led to frequent and costly maintenance and renewal operations for railway stakeholders. The substructure of the railway tracks, which serves as the foundation of the railway system, is a crucial and costly component in supporting the railway infrastructure (Shaltout et al., 2015). Ballasted track is the traditional and widely used railway track system worldwide. The subsurface drainage system, one of the components of the ballasted railway substructure (which includes ballast, sub-ballast, subgrade layers, and drainage system), plays a critical role in ensuring the healthy performance of the railway track. The effectiveness and efficiency of a ballasted railway track substructure primarily depend on the drainage system's ability to drain, divert, and remove water from the track substructure.

Malfunctioning, silting, and clogging of drainage systems can trap water in the substructure layers, resulting in frequent damage to the substructure by creation of weakened zones in the ground and around the drainage pipes. One important form of ground subsurface erosion caused by water leakage, is the weakening of soil zones around sewerage pipes, culverts, and drainage pipes. This erosion can lead to excess pore water pressure, localized settlement, instability, and eventual failure of the railway track substructure (Beckedahl, 1996; Sañudo et al., 2019). The aging of infrastructure, along with the formation of cracks and defects in buried pipes, increases the likelihood of water flow in the soil layer, washing away soil particles and necessitating emergency track maintenance (Kargah-Ostadi & Stoffels, 2015; Sharpe, 2000). Furthermore, the increasing axle loads, development of high-speed trains, climate change impact, year-on-year aging, and poor drainage conditions contribute to the gradual degradation of track substructures (Bačić & Juzbašić, 2020). Previous studies have observed that a significant portion of railway maintenance costs are associated with substructure layers and drainage issues (Tennakoon et al., 2012).

In the UK railway track system, inadequate drainage is a challenging risk factor that is likely to result in track failure and deformation. The UK railway network is classified as an aging-built

infrastructure, and its drainage systems were constructed without appropriate long-term design guidelines (Spink et al., 2014). Subsurface drainage networks are more complex than surface networks, and their design and condition assessment require detailed geotechnical and hydrological information (Hasnayn, 2016). However, current technologies for condition assessment of railway track drainage systems are limited, and they do not provide sufficient information for conclusive assessments of damage and deterioration (Wu et al., 2021). One of the significant challenges faced by Network Rail, the owner of most of the UK's railway infrastructure, is a lack of knowledge about the current condition of its drainage networks (Wu et al., 2021). Various studies have identified inadequate drainage as the primary cause of railway track instability and the root of most railway track malfunction-related issues (Li et al., 2015; Sañudo et al., 2019). Therefore, frequent monitoring and condition assessment of the railway track substructure and detection of progressive weakened zones are critically important. Early identification of anomalies or soil weakened zones caused by poor, ineffective, and aged drainage systems assist asset owners in developing planned maintenance programs (Bush III & Alexander, 1985). Conventional inspection methods for substructure condition assessment, and specifically for drainage pipe condition assessment, rely on visual inspection techniques (Koch et al., 2015). However, detecting local weakened zones in the ground and/or any defect in the drainage pipes using visual inspection is difficult because they are not visible. Additionally, these methods cannot determine the size of a local weakened zone or detect the possibility of weakened zone formation adjacent to drainage pipes (Wang et al., 2022). To address these limitations, non-destructive tests (NDTs) have been developed to assess the condition of buried infrastructure, including subsurface drainage pipes, and to investigate and detect local weakened zones in roads, pavements, shallow surfaces, and urban buried utilities (Costello et al., 2007; Liu & Kleiner, 2014; Xu et al., 2014).

In recent years, various techniques for the condition assessment of railway track substructures have been proposed (Artagan et al., 2020). Ground penetrating radar (GPR) is a highly effective and widely used geophysical non-destructive testing technique for subsurface investigation. It has been successfully applied in pavement condition assessment since the 1980s and has proven

effective in locating buried infrastructure such as pipes and cables, as well as detecting local structural weak zones in pavement substructure (Chen & Wimsatt, 2010; Evans et al., 2008; Plati & Dérobert, 2015). GPR was first used to investigate railway track substructures in 1985, but its results should be supported by data from other NDTs, such as Falling Weight Deflectometer (FWD) and Interferometric Synthetic Aperture Radar (InSAR), or destructive techniques like coring, to improve defect detection and validate GPR results (Evans et al., 2008; Ferrante et al., 2021; Tosti et al., 2020). Despite its wide range of applications, GPR has limitations. Interpretation of GPR test results requires substantial knowledge and experience, and the water content of substructure layers significantly impacts the quality of GPR data (Evans et al., 2008; Hunaidi, 1998). Seismic surface wave methods have been employed in geophysics, geotechnical site investigation, pavement and railway subsurface characterization, and anomaly detection (Barta, 2010; Foti et al., 2014; Sussmann Jr et al., 2017; Tamrakar et al., 2017). However, these methods are time-consuming and require complicated interpretation, relying on the engineer's judgment and experience (Anbazhagan et al., 2011). Infrared Thermography (IRT) is a new technique used for railway track substructure inspection, providing full-field data and real-time condition assessment (Kim, 2019). However, IRT is limited by weather conditions and requires a clear view between the infrared camera and the target surface (Clark et al., 2004; Janků et al., 2019). The ultrasonic technique is based on the travel time of acoustic waves that penetrate the ground and reflect from the buried pipe wall to the ground surface, detecting cracks, corrosion, and voids around pipes (Sheth & Sinfield, 2018). However, this technique is sensitive to soil and mud that may be attached to the pipe and requires thorough cleaning before inspection (Yu et al., 2021).

Although several techniques are available for ground condition assessment and buried utilities detection, railway substructure layers have received less attention, either for general railway track condition assessment or the detection of potential weakened zones in the ground due to drainage malfunction. The track modulus, a key stiffness characteristic of a railway track, can be used to determine the structural condition of a railway track substructure (Ebersöhn & Selig, 1994; Rezaei Tafti, 2018; Rogers et al., 2012; Wehbi, 2016). Falling weight deflectometer

(FWD) is a well-established NDT used to measure track modulus of railway substructures (Burrow et al., 2007). The FWD test was originally developed as a pavement condition assessment technique, FWD has been adapted for the railway industry to assess the condition of railway foundation and the presence of anomalies in the foundation layers (Burrow et al., 2007; Sharpe, 2000). The back-analysis technique is used to interpret FWD deflection basin data for estimating the moduli of substructure components in order to assess the condition of railways and pavements (Lee, 1988). Recently, Fathi et al. (2023) developed a back-analysis technique based on FWD testing data, which can estimate the stiffness moduli of the ballasted railway track substructure with high accuracy. However, to date, there is no method available to detect local anomalies, such as a ground weakened zone due to drainage malfunction, in the railway track substructure.

This paper presents a novel hybrid back-analysis technique to detect weakened zones in railway track substructures caused by drainage malfunctions, based on FWD test data, filling a significant gap where no existing solutions are available. Additionally, recent advancement in optimisation strategies provide a robust framework that can be adapted to enhance the proposed technique (Meng et al., 2023; Yang et al., 2023; Yang et al., 2024). The method utilises an ANN surrogate model, trained on virtual experimental data from finite element simulations, and links it with a GA to optimise the fit between modelled and measured deflections. This combination of AI techniques represents a breakthrough in addressing complex geo-structural monitoring challenges.

The proposed approach was thoroughly validated, demonstrating its time efficiency and independence from initial seed modulus values. By integrating advanced numerical simulations with data-driven optimisation, this technique overcomes the limitations of conventional methods, which often require more computational resources and lack flexibility. The proposed technique can significantly enhance the accuracy of railway substructure assessments while reducing the time required for analysis. This method has the potential to transform maintenance strategies for railway stakeholders, providing long-term benefits in operational safety and cost-efficiency.

1 Methodology

1.1 Overview of the model development procedure

The schematic of the methodology sequences used in this research is shown in Figure 1. Further details of the methodology will be presented in the following sections.

1.2 Development of finite element (FE) model

A finite element (FE) model of a railway track substructure was created using COMSOL Multiphysics to include a buried drainage pipe and a weakened zone adjacent to the pipe, under FWD test (COMSOL, 2015). The FE forward model developed by the authors was adapted and extended for this purpose (Fathi & Mehravar, 2022). In this study, the term weakened zone is used to refer to a zone of lower stiffness compared to the surrounding ground around the buried drainage pipe in the substructure. Further details of the FE model will be discussed in the subsequent sections.

1.2.1 Model geometry, material properties and boundary conditions

Figure 2 illustrates the cross-section of the railway track substructure, including a drainage pipe and a weakened zone adjacent to it. The thickness and material type of the substructure layers were determined based on the cone penetration test (CPT) results reported by Brough et al. (2006). The drainage pipe was modelled as a central subsurface drainage concrete pipe with an inner diameter of 600 mm and a thickness of 70 mm, buried at a depth of 1.65 m below the railway surface (Liedberg, 1991). This design aligns with the recommendations of the UK Network Rail Standards (NR/L2/CIV/003). The location of the drainage pipe was chosen to be under the FWD loading centre based on the results of preliminary simulations, which showed that the FE model is sensitive to the presence of a weakened zone in this location.

Figure 3 shows a typical Falling Weight Deflectometer (FWD) test setup (Burrow et al., 2007). In this setup, four geophones are positioned at varying distances from the centre of the loading plate. Geophone 1, located at the centre of the loading plate (referred to as the loading point),

measures the maximum deflection directly below the loading point (D_0). Geophone 2, located 300 mm from the loading point, records the maximum deflection at this distance, referred to as D_{300}. Geophones 3 and 4, positioned 1000 mm and 1500 mm from the loading point respectively, capture the maximum deflections at their respective distances, labelled as D_{1000} and D_{1500}.

For further clarification of the FWD testing configuration designed for railway application (Burrow et al., 2007) which is used in this study, a plan view of the problem is shown in Figure 4. In this research, we used numerical modelling to replicate a railway track, based on the cross-section outlined in Figure 2 and the test setup shown in Figure 4, and recorded the deflection basins at four geophone locations.

Three-dimensional (3D) model of the problem was simulated using COMSOL Multiphysics. Due to the symmetrical nature of the problem and to reduce computation time, only a quarter of the problem was modelled and shown in Figure 5(a). A close-up view of FWD geophone locations or datapoints is also presented in Figure 5(b).

Figure 6(a-b) depicts a drainage pipe and a weakened zone around it (Xu et al., 2017). To introduce a weakened zone into the FE model, five geometric parameters were defined: (i) expansion angle of the zone (θ); (ii) location of the zone around the pipe cross-section with respect to the vertical axis (α); (iii) depth of the zone (W_D); (iv) length of the weakened zone aligned with the track direction (W_L) and (v) longitude distance (along y axis) of the weakened zone from the centre of the loading point (Y_W). Three different possible positions were considered for α (Figure 6(a)), with the centre of the weakened zone located at 0°, 90°, and 180° relative to the vertical axis, which represents the weakened zones at the crown, springline and invert, respectively (Figure 6(a)).

In the FE model, quadratic brick elements were used to model the ballast, sub-ballast, and subgrade layers. However, due to the irregular geometry of the slope side of the ballast layer, the drainage pipe, and the weakened zone, tetrahedral elements were employed to model these sections. To eliminate the effect of shear wave reflection from the outer boundaries, a sufficiently large model size was considered in the FE simulations. The dimensions of the model were calculated based on the subgrade shear wave velocity, estimated using Equation 1, and the analysis of the distance travelled by the subgrade shear wave during the FWD test (Davis & Selvadurai, 2005). In this Equation, E is the layer modulus, ν is Poisson's ratio, and ρ is the material density.

$$V_s = \sqrt{\frac{E}{2(1+\nu)\rho}} \tag{1}$$

The analysis indicated that the horizontal dimension of the model perpendicular to the track (in the x direction) should be at least 9.25 m, while the dimensions in the y and z directions should be at least 8.7 m. Therefore, a 10 m x 10 m x 10 m geometry was chosen to prevent wave reflection from the outer boundaries and to avoid boundary effects on the surface deflection calculations. The bottom of the model was fixed in all three directions (x, y and z), and a symmetry boundary condition was applied to both the near-end perpendicular and left-sided planes parallel to the track direction- see Figure 5(a-b). Additionally, the roller boundary condition was assigned to both the right side and the far end of the model boundaries. A 31.25 kN load, a quarter of the FWD load magnitude, was defined using an idealized haversine function with 40 milliseconds' (ms) duration. This loading point was applied to the sleeper at the same location as the geophone D_0 (Figure 5(b)).

The material properties of the substructure layers, drainage pipe, and weakened zone included in the FE model were defined using a linear elastic material model and presented in Table 1.
It should be noted that a range of more complex constitutive models but found that the material non-linearity had minimal to no impact on the results. This finding aligns with the majority of

reports in the literature, where a linear-elastic material model has been successfully used in back-calculation algorithms for other linear infrastructure, such as roads and railways. Additionally, this assumption is justified due to the small deflections observed during the FWD test, which indicate that the material behaviour remains largely within the elastic zone (Sadrossadat et al., 2020). Furthermore, employing a linear-elastic material model significantly reduces the computational cost of the FE simulations, which is a critical factor when dealing with large-scale or complex models. In this case, the elastic modulus is the dominant parameter governing the material's behaviour.

It's important to mention that the layer modulus of the weakened zone was varied from 5% to 50% (specifically 5%, 10%, and 15%) of the subgrade 1 layer modulus to accommodate the impact of drainage defects on ground weakness and different scenarios were defined (Kaynia et al., 2017). Furthermore, the variation in the modulus of the weakened zone provides an opportunity to study the effects of different degrees of soil degradation (weakness) on the railway track's response to the FWD loading.

1.2.2 Sensitivity analysis of the FE model

This section presents the results of a series of sensitivity analyses conducted on the developed FE model. The aim was to observe the effects of the size and location of the weakened zone on the track surface deflections under FWD load at the four geophone locations. To this end, various weakened zones, were simulated as semi-circular shapes as presented in Figure 6(b), with different values of θ (weakened zone expansion angle) and α (location of the zone around the pipe cross-section with respect to the vertical axis). Different α values of 0°, 90°, and 180° were considered, representing the weakened zone positions at the crown, springline, and invert, respectively. θ values of 90°, 120°, and 150° were used to define the extent of the weakened zones (Figure 7). These parameters for the weakened zone were informed by literature (Li et al., 2021; Xu & Shen, 2020; Xu et al., 2017). Figure 7 presents a schematic of the drainage pipe and the weakened zone located at the pipe crown with various θ.

Table 2 shows the predicted deflections at four specific locations (D_0, D_{300}, D_{1000} and D_{1500}) across various weakened zone scenarios examined in this sensitivity analysis. This table also shows the predicted deflection values under FWD testing condition for each scenario, alongside deflections from the reference scenario that does not include a weakened zone. The average percentage error presented in Table 2 highlights the variation in deflections relative to the reference scenario, illustrating the impact of the weakened zone on surface deflections.

The outcomes of this sensitivity analysis (Table 2) revealed that the presence of the weakened zone at the drainage pipe's crown (α = 0) resulted in the largest track surface deflection at D_0, D_{300}, D_{1000} and D_{1500} compared to the weakened zone at the invert and springline. In addition, θ also influenced the track surface deflection at defined deflection measurement points. As θ increased, the surface deflection at the basin increased. This was expected because a larger θ means there is a greater weakened zone in the substructure. It can be observed that the weakened zone at the invert of the drainage pipe (α = 180°) with width values of 90°, 120°, and 150° resulted in the minimum average discrepancy, ranging from approximately 0.1% to 0.2%, when compared with the reference model. Conversely, the weakened zone at the crown (α = 0°) with a width of 150° caused an average discrepancy of about 0.9%.

As shown in Figure 8, this sensitivity analysis demonstrates that the critical position of the weakened zone is at the crown of the drainage pipe. In other words, the probability of detecting a weakened zone is highest when it is positioned at the crown of the drainage pipe. Based on these finding, for the remainder of the study, including data generation for ANN training, this critical weakened zone position around the drainage pipe is considered, as presented in Figure 6b.

Figure 8: Effect of the expansion angle and position of the weakened zone around the pipe on the track surface deflection

Additionally, further sensitivity analysis on the FE model was conducted to investigate the effect of three geometric characteristics of the weakened zone— W_D, W_L, and Y_W —on the predicted

deflection values under FWD testing conditions. For this investigation, different combinations of the values presented in Table 4 for the weakened zone's geometric characteristics (W_D, W_L, and Y_W) were considered. The results indicate that W_D is the most influential parameter on the predicted deflections and Y_w is the least influential. It was observed that weakened zones with W_D and W_L less than 15 cm and 20 cm, respectively, are less detectable by the developed back-analysis technique.

1.2.3 Synthetic database generation

An artificial neural network (ANN) was developed and trained as a surrogate forward model to replace the FE model as FE simulation needs significantly computation time (Luo et al., 2024; Meng et al., 2024). The ANN was trained to identify correlations between the substructure properties, weakened zone specifications, and surface deflections of the FWD, effectively mimicking the FE model's behaviour. The trained ANN surrogate model served as the objective function in the back-analysis technique. To train the ANN surrogate forward model, a synthetic database comprising inputs and corresponding outputs was generated using the FE model developed in the previous section. The database contains a total of 1,002 deflection basins, including deflection values at four datapoints (D_0, D_{300}, D_{1000} and D_{1500}) under various ground conditions. These conditions include different values for substructure layer moduli, weakened zone modulus, size and location of the weakened zone (W_D, W_L and Y_W) in the substructure. The database was generated using LiveLink COMSOL with MATLAB to achieve efficient computational time for data generation. It includes all combinations of W_D, W_L and Y_W, as well as the E_W and E_2 to E_6 values, and the reference scenario of a five-layer railway substructure with a drainage pipe and no weakened zone. The critical case, which had a weakened zone with a geometry of $\theta = 150°$ positioned at $\alpha = 0°$ (the pipe crown), was included and kept constant in the database based on parametric analysis results for various weakened zone geometries.

The input variables for the ANN included the substructure layer properties and weakened zone specifications, while the outputs were the peak surface deflections at four datapoints (D_0, D_{300}, D_{1000} and D_{1500}). The input variable ranges for the substructure layers (clean ballast,

contaminated ballast, subgrade 1, subgrade 2, and subgrade 3) were 70-170 MPa, 20-50 MPa, 50-100 MPa, 15-50 MPa, and 100-400 MPa, respectively. The range of weakened zone moduli (E_W) was 5%-50% of E_4 (5%, 10%, 15%, 20%, 30%, 40%, and 50%). The geometrical properties of the weakened zone were varied as follows: W_D = [0, 7.5, 10, 15, 20 cm], W_L = [0, 20, 40, 60 cm], and Y_W = [0, 0.15, 0.65, 1.25, 1.6375 m]. The weakened zone properties were based on recommendations from the literature (Kaynia et al., 2017; Meguid & Kamel, 2014).

1.2.4 ANN architecture and training

The ANN architecture needs to be defined prior to the ANN training process. In order to decide on the type of neural network for this study an investigation study was conducted by testing a multilayer perceptron (MLP) feed-forward neural network to develop the back-analysis technique. Table 3 presents the of root mean squared error (RMSE) of the ANN estimates and target values of the surface deflections (i.e., D_0, D_{300}, D_{1000} and D_{1500}) for some of the ANN architectures that were tested. The high value of RMSE shows that the MLP network was not able to predict surface deflections accurately, especially for D_0.

For this reason, in this study, the radial basis function (RBF), a type of feed-forward neural network commonly used for function approximation, classification, and regression, was employed (Leonard et al., 1992). In the RBF, each neuron in the hidden layer has an activation function known as a basis function, and the hidden layer serves both computational and training functions (56). Gaussian RBF was used as the basis function in the current analysis, as it is the most commonly employed type of RBF. The relatively straightforward architecture of this network facilitates quicker and more efficient training compared to other types of neural networks. Additionally, it possesses a superior ability to approximate functions for nonlinear data (Gajewski & Sadowski, 2014; Yu et al., 2011). The RBF comprises only one hidden layer, which consists of several hidden neurons. Each neuron in the hidden layer has an activation function, also known as a basis function. The Gaussian RBF is a radial function that depends on the distance between the input point and the centre point. It is calculated using Equation 2.

$$\varphi_j(x, c_j) = exp(\frac{-\|x - c_j\|^2}{2\sigma_j{}^2}) \quad (2)$$

where,

x is the n-dimensional input vector

c_j is the centre of RBF for hidden neuron j

$\|x - c_j\|$ is the Euclidean distance between the centre of the RBF and the input

σ_j is the width of Gaussian function.

The number of neurons in the input layer corresponds with the number of inputs in the problem. For this problem, the ANN was fed with 19 inputs. These inputs encompassed the mechanical properties of the railway track substructure, including the elastic modulus (E_1-E_6), Poisson's ratio (ν_1-ν_6), and the thickness of the layers (t_1-t_6). Additionally, the mechanical and geometrical parameters of the weakened zone were included, namely the elastic modulus of the weakened zone (E_w), weakened zone expansion angle (θ) of 150°, W_D, W_L, Y_W, and the FWD loading magnitude (as shown in Tables 4 and 5).

All combinations of W_D, W_L, Y_w, employed in the training database are presented in Table 5.

Additionally, the reference scenario, consisting of a five-layer railway substructure with a drainage pipe and no local weakened zone adjacent to the pipe, was included in the database. Based on the sensitivity analysis results (section 2.2.2), a weakened zone with θ = 150° positioned at α = 0° (the pipe crown) was selected, and various values of E_2 to E_6, layer thicknesses, drainage pipe diameters, E_W, and weakened zone geometrical properties, including W_D, W_L and Y_W, were employed to generate a comprehensive set of scenarios. The outputs of the ANN were the surface deflections corresponding to the number of predefined geophones at different offsets from the FWD loading point (4 geophones- see Figure 3 and 4).

The training process of the RBF network consists of two main steps. The first step is to specify the centres (c_j) and widths of the basis functions in the hidden layer (σ_j). Once these parameters have been calculated, the output of each hidden neuron in the hidden layer is linearly scaled by its corresponding connecting weight to the output neuron. The output of the network is then calculated by summing the outputs of the hidden neurons. Equation 3 shows the calculation of the network output, where w_j is the weight of the connection between hidden neuron *j* and the output neuron, *b* is the bias, *k* is the basis centre and φ_j is the Gaussian RBF function (Govindaraju, 2000).

$$F_x = \sum_{j=1}^{k} w_j \varphi_j(x, c_j) + b \qquad (3)$$

where,

w_j is weight

b is the bias

K is the basis centres

φ_j is Gaussian RBF

The main parameters of the RBF network include a matrix of input vectors, a matrix of output vectors, the mean square error (MSE) function, the spread of RBF, and the number of neurons to be added at each iteration. More details on the RBF network can be found in (Jinkun, 2013).

The number of neurons in the hidden layer is a key parameter that affects the performance of the RBF network. In this paper, a trial-and-error method was employed to determine the optimal number of hidden neurons for the RBF network. A total of 1,000 hidden neurons, with a training performance value of 1.185e−06, was found to be optimal. Moreover, the spread of the RBF, which controls the smoothness of the RBF, is another significant factor that affects the performance of the RBF network (Chang & Chen, 2003; Hamim et al., 2020). Therefore, different values of the RBF spread were tested to evaluate the performance of the RBF network. The range of tested values was from 1 to 10, with an increment of 1. The RBF network with a

spread value of 1 produced the lowest MSE, and thus, the RBF network with 1,000 hidden neurons and a spread value of 1 was selected. The structure of the ANN surrogate forward model is illustrated in Figure 9.

Once the training process of the RBF network was finished, the performance of the developed network was assessed using RMSE, and R. Figures 10(a-c) to 13(a-c) present the calculated deflections at four datapoints (D_0, D_{300}, D_{1000} and D_{1500}) using the ANN surrogate forward model.

The results obtained from the RBF network are presented in Figures 10(b), 11(b), 12(b), and 13(b), which show the R values of the network output at D_0, D_{200}, D_{1000} and D_{1500}, respectively. It can be observed that the R values were close to 1 for all calculated deflections, indicating a strong correlation between the predicted and actual deflections. The RMSE values and corresponding predicted deflections from the RBF network are presented in Figures 10(c), 11(c), 12(c), and 13(c). The RMSE values for D_0, D_{200}, D_{1000} and D_{1500} were 2.08e−03, 6.23e−04, 1.58e−04, and 1.03e−04, respectively. These results indicate that the RBF network was able to predict the deflections accurately for different measurement points. The high values of R and relatively small RMSE values demonstrate the satisfactory performance of the trained network in predicting the deflections accurately. Overall, these results suggest that the RBF network is a reliable and effective tool for predicting the deflection of railway substructure under FWD loading condition.

1.3 Development of hybrid ANN-GA back-analysis technique for local anomaly detection

In this stage, an optimization tool in the form of a single-objective GA was integrated with the ANN surrogate forward model. The integration of a GA as an optimization technique can eliminate the need to define layer seed moduli (the inputs to the ANN) at the start of each iteration, and in this study, it was used to find the optimum values for unknown parameters such

as substructures' layer moduli (E_2 to E_6), local weakened zone modulus (E_W), and its geometric properties (W_D, W_L and Y_W). The use of a GA and ANN integration has been shown to provide a robust solution to complex optimization problems (Javadi et al., 2005). To solve the current optimization problem, a deflection-based objective function (Equation 4) was chosen as (Ghorbani et al., 2020; Gopalakrishnan & Khaitan, 2010):

$$Fitness\ Function = \sqrt{\frac{1}{n}\sum_{i=1}^{n}((D_i - d_i)/d_i)^2} \times 100 \quad (4)$$

where D_i and d_i are the calculated and measured values of the deflections, respectively, and n is the number of measurement points.

The developed back-analysis technique incorporates a detailed GA optimization process, as illustrated in Figure 14 (Fathi et al., 2023). The GA initially generates a set of random values for the unknown parameters, and the ANN calculates the surface deflections at the four geophone locations. Subsequently, the differences between the calculated and measured deflection values are evaluated using the defined fitness function (Equation 3). The roulette wheel selection function is employed to choose the best values, which are then used to produce the next generation through the mutation and crossover operators. This process is iterated until the RMSE for any of the estimations falls below a pre-established error tolerance, or until the maximum number of generations has been reached. The error tolerance threshold was determined based on the geophones' accuracy, which is equivalent to 0.001 mm.

It should be noted that the GA parameters used in this study were specifically tailored to the problem being addressed. To ensure accurate and efficient computation, it was necessary to determine the optimal values for these parameters. A sensitivity analysis was conducted to determine the appropriate population and generation sizes for the GA. Figure 15 illustrates the results of this sensitivity analysis, which shows the variation of RMSE values with the

generation size for different population sizes ranging from 80 to 300. The results indicate that a population size of 200 and a generation size of 300 produced the minimum RMSE, thus indicating that these parameters were optimal. Therefore, the adopted GA parameters were a population size of 200, a generation size of 300, a crossover probability of 0.8, and a mutation probability of 0.1.

1.4 Results and Discussions

Firstly, a parametric analysis was conducted to assess the impact of variations in size of the weakened zone (W_L) and its longitudinal distance from the loading point (Y_W) on the performance of the ANN-GA back-analysis. To investigate the impact of each W_L and Y_w individually, various scenarios were defined. Based on the assumed 0.001 mm measurement accuracy of the geophones, differences in deflections exceeding this value were considered meaningful and included in the analysis, while differences less than this value were excluded as noise. Additionally, a critical threshold was established to determine the point at which differences between the geophones' measurements and the reference deflection (in the absence of a weakened zone) reached 0.001 mm, equivalent to the geophones' accuracy. This threshold resulted in an RMSE of 0.1%. This threshold is visually represented by a dashed red line in Figures 16 and 17, which serves as the boundary for the applicability and reliability of the back-analysis technique.

To investigate the impact of the weakened zone size on the technique’s performance, we examined three distinct values for W_D, maintaining Y_w constant at zero and changed W_L. For each W_D value, we evaluated technique performance across various W_L values: 20 cm, 40 cm, and 60 cm. The results, presented in Figure 16, indicate that the size of the weakened zone significantly impacts the accuracy of the technique. Generally, as the size of the weakened zone (W_L) increases, the technique's ability to predict the geometry of the weakened zone also improves. This figure indicates that if the length of the weakened zone (W_L) is relatively small (e.g., 20

cm), then the minimum size of W_D must be approximately 13 cm to be detectable by the developed technique.

Figure 17 illustrates how the distance of the weakened zone (Y_w) from the loading point affects prediction accuracy. The analysis includes four Y_w values: 0 cm, 15 cm, 125 cm, and 163.75 cm based on the longitudinal geophone arrangement in Figures 5 and 6. As the distance increases, prediction accuracy decreases, but all RMSE values remain above the threshold. Additionally, the weakened zone size (W_D) improves accuracy, especially when W_D is 15 cm or more. Thus, the longitudinal geophone arrangement shown in Figures 4 and 5 is effective for detecting substructure anomalies. It was observed that detectability decreased as Y_W increased, except for Y_W = 15 cm. In addition to the deflection values, various weakened zone specifications, including Y_W, affect the shape of the deflection basin and the peak deflection. Because of the specific configuration of the geophones and their distancing, the peak of the deflection basin may not be captured by the geophone, which results in the exception mentioned above at Y_W = 15 cm.

2.4.1 Validation of the developed ANN-GA back-analysis technique

To validate the accuracy and performance of the developed ANN-GA back-analysis technique, we applied it to six distinct cases involving weakened zone mechanical properties and geometries, which we refer to as case studies. These cases vary in their geometrical characteristics (W_D) and layer modulus (E_W) of weakened zone (Table 6) while other parameters including W_L, Y_W, α and θ were kept contact. Full details of the weakened zones' characteristics in these case studies are presented in Table 6. In these case studies, the combination of 7.5 cm and 20 cm as maximum and minimum values of W_D were considered, along with different values of E_W (i.e., 25% E_4, 35% E_4, and 50% E_4) and constant values of 60 cm and 15 cm for W_L, and Y_W, respectively. As mentioned earlier in section 2.2.2, W_D has the greatest impact on deflections compared to W_L, and Y_W, so the two variation of this parameter was considered using the minimum and maximum values for W_D.

The results of these scenarios are presented in Table 7. It can be seen that the developed back-analysis technique can predict various weakened zone moduli accurately when a larger area around the drainage pipe is affected by a drainage defect - with higher values of W_D. For example, when W_D is 20 cm, the technique can accurately predict the weakened zone moduli for all three cases, with the error being less than 10 % in each instance (as shown by the discrepancy in Table 6). In other words, in these cases, represented by case studies 2, 4, and 6, the back-analysed value for E_W is more accurate compared to case studies 1, 3, and 5, which have smaller geometrical properties of the weakened zone. This can be attributed to the fact that weakened zones with W_D and W_L less than 15 cm and 20 cm, respectively, are less detectable by the developed back-analysis technique.

Additionally, this table shows the estimated values for E_W and the discrepancy (percentage error) for case studies 1 to 6. The estimated E_W values for case studies 2, 4, and 6, with W_D=20 cm, exhibited discrepancies of less than 10%, specifically 8.90%, 7.68%, and 5.49%, respectively. In contrast, the estimations for case studies with W_D=7.5 cm showed discrepancies of up to 41.51%. This discrepancy can be attributed to the significant influence of W_D as a critical parameter of the weakened zone, as discussed in section 2.2.2. Moreover, for weakened zones with W_D = 20 cm and E_W ranging between 25% and 50% of $E4$, the developed back-analysis technique accurately predicts W_D, W_L, Y_W, and E_W.

Conclusions

The following key conclusions are drawn from the research:

- The proposed back-analysis technique is applicable to detecting soil weakened zone caused by subsurface drainage networks in railway substructure.
- The use of the RBF network as a forward surrogate model to calculate railway track surface deflection using FWD testing data was successful.

- The developed ANN-GA back-analysis technique demonstrated reliable performance in estimating substructure layer moduli (E_2 to E_6) and the weakened zone modulus (E_W), with error values consistently below 10%. This high level of accuracy was observed particularly when the weakened zone depth (W_D) was 20 cm, underscoring the robustness and effectiveness of the model.
- The ANN-GA back-analysis technique showed efficient computational time where the maximum computational time was recorded as 792 seconds observed for case study 1 (Table 6).
- Parametric studies indicated that the back-analysis technique is more effective with larger weakened zone depth (W_D) and length (W_L).
- It was observed that if the length of the weakened zone (W_L) is relatively small (e.g., 20 cm), then the minimum size of W_D must be approximately 13 cm to be detectable by the developed technique.
- The technique's prediction accuracy declines as the weakened zone is located farther from the loading point, though RMSE values remain above the threshold. When the size of the weakened zone is around 15 cm or more, accuracy improves for these farther distances.
- The longitudinal geophone arrangement in Figures 4 and 5 is effective for detecting substructure anomalies.

References

Anbazhagan, P., Lijun, S., Buddhima, I., & Cholachat, R. (2011). Model track studies on fouled ballast using ground penetrating radar and multichannel analysis of surface wave. *Journal of Applied Geophysics*, *74*(4), 175-184.

Artagan, S. S., Bianchini Ciampoli, L., D'Amico, F., Calvi, A., & Tosti, F. (2020). Non-destructive assessment and health monitoring of railway infrastructures. *Surveys in Geophysics*, *41*(3), 447-483.

Bačić, M., & Juzbašić, A. (2020). Challenges of Railway Embankments Remediation.

Barta, J. (2010). A methodology for geophysical investigation of track defects. *Proceedings of the Institution of Mechanical Engineers, Part F: Journal of Rail and Rapid Transit*, *224*(4), 237-244.

Beckedahl, H. R. (1996). *Subsurface soil erosion phenomena in Transkei and southern KwaZulu-Natal, South Africa*

Burrow, M. P., Chan, A. H., & Shein, A. (2007). Deflectometer-based analysis of ballasted railway tracks. *Proceedings of the Institution of Civil Engineers-Geotechnical Engineering*, *160*(3), 169-177.

Bush III, A. J., & Alexander, D. R. (1985). *Pavement Evaluation Using Deflection Basin Measurements and Layered Theory (Discussion and Closure)*.

Chang, F.-J., & Chen, Y.-C. (2003). Estuary water-stage forecasting by using radial basis function neural network. *Journal of Hydrology*, *270*(1-2), 158-166.

Chen, D. H., & Wimsatt, A. (2010). Inspection and condition assessment using ground penetrating radar. *Journal of geotechnical and geoenvironmental engineering*, *136*(1), 207-214.

Clark, M., Gordon, M., & Forde, M. C. (2004). Issues over high-speed non-invasive monitoring of railway trackbed. *Ndt & E International*, *37*(2), 131-139.

COMSOL, M. (2015). Comsol multiphysics user guide (version 5.2). *COMSOL, AB*, 5-437.

Costello, S., Chapman, D., Rogers, C., & Metje, N. (2007). Underground asset location and condition assessment technologies. *Tunnelling and underground space technology*, *22*(5-6), 524-542.

Davis, R. O., & Selvadurai, A. P. (2005). *Plasticity and geomechanics*. Cambridge university press.

Ebersöhn, W., & Selig, E. T. (1994). Track modulus measurements on a heavy haul line. *Transportation research record*, *1470*, 73.

Evans, R. D., Frost, M. W., Stonecliffe-Jones, M., & Dixon, N. (2008). A review of pavement assessment using ground penetrating radar (GPR).

Fathi, S., & Mehravar, M. (2022). A Back-Analysis Technique for Condition Assessment of Ballasted Railway Tracks. In *Advances in Transportation Geotechnics IV* (pp. 931-941). Springer.

Fathi, S., Mehravar, M., & Rahman, M. (2023). Development of FWD based hybrid back-analysis technique for railway track condition assessment. *Transportation Geotechnics*, *38*, 100894.

Ferrante, C., Bianchini Ciampoli, L., Benedetto, A., Alani, A. M., & Tosti, F. (2021). Non-destructive technologies for sustainable assessment and monitoring of railway infrastructure: a focus on GPR and InSAR methods. *Environmental Earth Sciences*, *80*(24), 1-20.

Foti, S., Lai, C. G., Rix, G. J., & Strobbia, C. (2014). *Surface wave methods for near-surface site characterization*. CRC press.

Gajewski, J., & Sadowski, T. (2014). Sensitivity analysis of crack propagation in pavement bituminous layered structures using a hybrid system integrating Artificial Neural Networks and Finite Element Method. *Computational Materials Science*, *82*, 114-117.

Ghorbani, B., Arulrajah, A., Narsilio, G., Horpibulsuk, S., & Bo, M. W. (2020). Development of genetic-based models for predicting the resilient modulus of cohesive pavement subgrade soils. *Soils and Foundations*, *60*(2), 398-412. https://doi.org/10.1016/j.sandf.2020.02.010

Gopalakrishnan, K., & Khaitan, S. K. (2010). Development of an intelligent pavement analysis toolbox. Proceedings of the Institution of Civil Engineers-Transport,

Govindaraju, R. S. (2000). Artificial neural networks in hydrology. I: Preliminary concepts. *Journal of Hydrologic Engineering*, *5*(2), 115-123.

Gunn, D., Chambers, J., Dashwood, B., Lacinska, A., Dijkstra, T., Uhlemann, S., Swift, R., Kirkham, M., Milodowski, A., & Wragg, J. (2018). Deterioration model and condition monitoring of aged railway embankment using non-invasive geophysics. *Construction and Building Materials*, *170*, 668-678.

Hamim, A., Yusoff, N. I. M., Omar, H. A., Jamaludin, N. A. A., Hassan, N. A., El-Shafie, A., & Ceylan, H. (2020). Integrated finite element and artificial neural network methods for constructing asphalt concrete dynamic modulus master curve using deflection time-history data. *Construction and Building Materials*, *257*, 119549.

Hasnayn, M. M. (2016). *Railway subgrade behaviour under flood conditions: an experimental study at full-scale* Heriot-Watt University].

Hunaidi, O. (1998). Ground-penetrating radar for detection of leaks in buried plastic water distribution pipes. Proceedings of the seventh international conference on Ground Penetrating Radar, 1998,

Janků, M., Cikrle, P., Grošek, J., Anton, O., & Stryk, J. (2019). Comparison of infrared thermography, ground-penetrating radar and ultrasonic pulse echo for detecting delaminations in concrete bridges. *Construction and Building Materials*, *225*, 1098-1111.

Javadi, A. A., Farmani, R., & Tan, T. P. (2005). A hybrid intelligent genetic algorithm. *Advanced Engineering Informatics*, *19*(4), 255-262.

Jinkun, L. (2013). Radial basis function neural network control for mechanical systems. *Tsinghua University Press, Beijing, China*, *10*, 978-973.

Kargah-Ostadi, N., & Stoffels, S. M. (2015). Backcalculation of flexible pavement structural properties using a restart covariance matrix adaptation evolution strategy. *Journal of Computing in Civil Engineering*, *29*(2), 04014035. https://doi.org/10.1061/(ASCE)CP.1943-5487.0000309

Kaynia, A. M., Park, J., & Norén-Cosgriff, K. (2017). Effect of track defects on vibration from high speed train. *Procedia Engineering*, *199*, 2681-2686.

Kim, J. (2019). Non-destructive characterization of railway materials and components with infrared thermography technique. *Materials*, *12*(24), 4077.

Koch, C., Georgieva, K., Kasireddy, V., Akinci, B., & Fieguth, P. (2015). A review on computer vision based defect detection and condition assessment of concrete and asphalt civil infrastructure. *Advanced Engineering Informatics*, *29*(2), 196-210.

Lee, S.-W. (1988). Backcalculation of pavement moduli by use of pavement surface deflections.

Leonard, J. A., Kramer, M. A., & Ungar, L. H. (1992). Using radial basis functions to approximate a function and its error bounds. *IEEE transactions on neural networks*, *3*(4), 624-627.

Li, B., Wang, F., Fang, H., Yang, K., Zhang, X., & Ji, Y. (2021). Experimental and numerical study on polymer grouting pretreatment technology in void and corroded concrete pipes. *Tunnelling and underground space technology*, *113*, 103842.

Li, D., Hyslip, J., Sussmann, T., & Chrismer, S. (2015). *Railway geotechnics*. CRC Press.

Liedberg, S. (1991). Earth pressure distribution against rigid pipes under various bedding conditions. Full-scale field tests in sand. *Chalmers Tekniska Hoegskola. Doktorsavhandlingar*.

Liu, Z., & Kleiner, Y. (2014). Computational intelligence for urban infrastructure condition assessment: Water transmission and distribution systems. *IEEE Sensors Journal*, *14*(12), 4122-4133.

Luo, C., Zhu, S.-P., Keshtegar, B., Macek, W., Branco, R., & Meng, D. (2024). Active Kriging-based conjugate first-order reliability method for highly efficient structural reliability analysis using resample strategy. *Computer Methods in Applied Mechanics and Engineering*, *423*, 116863.

Meguid, M. A., & Kamel, S. (2014). A three-dimensional analysis of the effects of erosion voids on rigid pipes. *Tunnelling and underground space technology*, *43*, 276-289.

Meng, D., Yang, H., Yang, S., Zhang, Y., De Jesus, A. M., Correia, J., Fazeres-Ferradosa, T., Macek, W., Branco, R., & Zhu, S.-P. (2024). Kriging-assisted hybrid reliability design and optimization of offshore wind turbine support structure based on a portfolio allocation strategy. *Ocean Engineering*, *295*, 116842.

Meng, D., Yang, S., de Jesus, A. M., & Zhu, S.-P. (2023). A novel Kriging-model-assisted reliability-based multidisciplinary design optimization strategy and its application in the offshore wind turbine tower. *Renewable Energy*, *203*, 407-420.

Plati, C., & Dérobert, X. (2015). Inspection procedures for effective GPR sensing and mapping of underground utilities and voids, with a focus to urban areas. In *Civil engineering applications of ground penetrating radar* (pp. 125-145). Springer.

Rezaei Tafti, S. (2018). *High Speed Train Geotechnics: Numerical and Experimental Simulation of Some Embankment Problems*

Rogers, C., Hao, T., Costello, S., Burrow, M., Metje, N., Chapman, D., Parker, J., Armitage, R., Anspach, J., & Muggleton, J. (2012). Condition assessment of the surface and buried infrastructure–A proposal for integration. *Tunnelling and underground space technology*, *28*, 202-211.

Sadrossadat, E., Ghorbani, B., Zohourian, B., Kaboutari, M., & Rahimzadeh Oskooei, P. (2020). Predictive modelling of the MR of subgrade cohesive soils incorporating CPT-related parameters through a soft-computing approach. *Road Materials and Pavement Design*, *21*(3), 701-719.

Sañudo, R., Miranda, M., García, C., & García-Sanchez, D. (2019). Drainage in railways. *Construction and Building Materials*, *210*, 391-412.

Shaltout, R., Ulianov, C., & Chen, H. (2015). Coupled numerical modelling of railway track substructure with vehicle-track interaction. *Civil-Comp Proceedings*, *108*.

Sharpe, P. (2000). Trackbed investigation. Permanent Way Institution Journal and Report of Proceedings,

Sheth, A., & Sinfield, J. V. (2018). Synthesis Study: Overview of Readily Available Culvert Inspection Technologies.

Spink, T., Duncan, I., Lawrance, A., & Todd, A. (2014). Transport infrastructure drainage: condition appraisal and remedial treatment. *CIRIA, London*, *2*, 391-412.

Sussmann Jr, T., Thompson II, H., Stark, T., Wilk, S., & Ho, C. (2017). Use of seismic surface wave testing to assess track substructure condition. *Construction and Building Materials*, *155*, 1250-1255.

Tamrakar, P., Azari, H., Yuan, D., & Nazarian, S. (2017). Implementation of spectral analysis of surface waves approach for characterization of railway track substructures. *Transportation Geotechnics*, *12*, 101-111.

Tennakoon, N., Indraratna, B., Rujikiatkamjorn, C., Nimbalkar, S., & Neville, T. (2012). The role of ballast fouling characteristics on the drainage capacity of rail substructure.

Tosti, F., Gagliardi, V., D'Amico, F., & Alani, A. M. (2020). Transport infrastructure monitoring by data fusion of GPR and SAR imagery information. *Transportation research procedia*, *45*, 771-778.

Wang, D., Moore, I. D., Hoult, N., & Lan, H. (2022). Evaluation and comparison of different detection technologies on simulated voids near buried pipes. *Tunnelling and underground space technology*, *123*, 104440.

Wehbi, M. (2016). *Developing a novel technique to extract track stiffness information from track geometry measurement* University of Birmingham].

Wu, Y., Tait, S., Nichols, A., & Raja, J. (2021). Simulation of Railway Drainage Asset Service Condition Degradation in the UK Using a Markov Chain–Based Approach. *Journal of Infrastructure Systems*, *27*(3), 04021023.

Xu, C., Chen, Q., Sun, F., & Chen, D. (2014). *Applications of electromagnetic waves for void and anomaly detections*. ASTM International.

Xu, M., & Shen, D. (2020). The influence of erosion voids on the longitudinal behaviour of a jointed large-diameter reinforced concrete pipeline. *Tunnelling and underground space technology*, *103*, 103494.

Xu, M., Shen, D., & Jin, D. (2017). The behaviour of jointed large-diameter reinforced concrete pipeline buried in various ground conditions. *Engineering Structures*, *153*, 354-369.

Yang, S., Meng, D., Guo, Y., Nie, P., & Jesus, A. M. d. (2023). A reliability-based design and optimization strategy using a novel MPP searching method for maritime engineering structures. *International Journal of Structural Integrity*, *14*(5), 809-826.

Yang, S., Meng, D., Wang, H., & Yang, C. (2024). A novel learning function for adaptive surrogate-model-based reliability evaluation. *Philosophical Transactions of the Royal Society A*, *382*(2264), 20220395.

Yu, H., Xie, T., Paszczyñski, S., & Wilamowski, B. M. (2011). Advantages of radial basis function networks for dynamic system design. *IEEE transactions on Industrial Electronics*, *58*(12), 5438-5450.

Yu, Y., Safari, A., Niu, X., Drinkwater, B., & Horoshenkov, K. V. (2021). Acoustic and ultrasonic techniques for defect detection and condition monitoring in water and sewerage pipes: A review. *Applied Acoustics*, *183*, 108282.

Accepted manuscript doi:
10.1680/jtran.23.00066

Tables

Table 1: Mechanical properties of the track and soil used to model the railway (Fathi et al., 2023)

	Properties	Value	Reference
Sleeper	Layer modulus, E_1 (GPa)	20.7	(Brough et al., 2006)
	Poisson's ratio, ν	0.15	(Burrow et al., 2007)
	Density, ρ (kg/m^3)	2,500	(Burrow et al., 2007)
	Damping ratio	0.05	(Haji Abdulrazagh et al., 2019)
Clean ballast (Ballast 1)	Layer modulus, E_2 (MPa)	110	(Brough et al., 2006)
	Poisson's ratio, ν	0.2	(Burrow et al., 2007)
	Density, ρ (kg/m3)	1,700	(Burrow et al., 2007)
	Damping ratio	0.05	(Wehbi et al., 2020)
Contaminated ballast (Ballast 2)	Layer modulus, E_3 (MPa)	32.25	(Brough et al., 2006)
	Poisson's ratio, ν	0.49	(Burrow et al., 2007)
	Density, ρ (kg/m3)	1,800	(Burrow et al., 2007)
	Damping ratio	0.05	(Wehbi et al., 2020)
Subgrade 1	Layer modulus, E_4 (MPa)	71.83	(Brough et al., 2006)
	Poisson's ratio, ν	0.49	(Burrow et al., 2007)
	Density, ρ (kg/m3)	1,900	(Burrow et al., 2007)
	Damping ratio	0.05	(Wehbi et al., 2020)
Subgrade 2	Layer modulus, E_5 (MPa)	33.96	(Brough et al., 2006)
	Poisson's ratio, ν	0.49	(Burrow et al., 2007)
	Density, ρ (kg/m3)	1,900	(Burrow et al., 2007)
	Damping ratio	0.2	(Wehbi et al., 2020)
Subgrade 3	Layer modulus, E_6 (MPa)	362.1	(Brough et al., 2006)
	Poisson's ratio, ν	0.49	(Burrow et al., 2007)
	Density, ρ (kg/m3)	1,800	(Burrow et al., 2007)
	Damping ratio	0.2	(Wehbi et al., 2020)
Weakness zone	Layer modulus, E_w (MPa)	5%–50% E_4	(Kaynia et al., 2017)
	Poisson's ratio, ν	0.49	(Burrow et al., 2007)
	Density, ρ (kg/m^3)	1,900	(Burrow et al., 2007)
	Damping ratio	0.2	(Wehbi et al., 2020)
Concrete drainage pipe	Layer modulus, E_P (MPa)	34,000	(Meguid and Kamel, 2014)
	Poisson's ratio, ν	0.2	(Meguid and Kamel, 2014)
	Density, ρ (kg/m^3)	2,600	(Meguid and Kamel, 2014)

Accepted manuscript doi:
10.1680/jtran.23.00066

Table 2: Outcomes of the FE sensitivity analysis - Exploring the influence of weakened zone expansion angle and position on track surface deflections

Expansion angle (θ)	Location (α)		Surface deflection (mm) (Geophones)				Average percentage difference
			D_0	D_{300}	D_{1000}	D_{1500}	
90	0	Crown	−1.607	−0.944	−0.322	−0.243	0.631
	90	Springline	−1.604	−0.941	−0.321	−0.243	0.4097
	180	Invert	−1.602	−0.938	−0.319	−0.242	0.102
120	0	Crown	−1.608	−0.945	−0.323	−0.244	0.776
	90	Springline	−1.605	−0.942	−0.322	−0.244	0.634
	180	Invert	−1.602	−0.939	−0.319	−0.243	0.183
150	0	Crown	−1.608	−0.946	−0.323	−0.244	0.898
	90	Springline	−1.607	−0.944	−0.324	−0.243	0.793
	180	Invert	−1.603	−0.939	−0.320	−0.243	0.227
Reference scenario (no void)			**−1.602**	**−0.938**	**−0.318**	**−0.242**	

Table 3: Trial-and-error process toward ANN architecture definition

ANN architectures	RMSE D_0	RMSE D_{300}	RMSE D_{1000}	RMSE D_{1500}
19-7-6-5-4	1.3273e−02	5.922e−03	3.8038e−03	2.532e−03
19-6-6-6-4	1.2918e−02	4.2687e−03	1.6709e−03	8.9329e−04
19-7-7-6-4	1.1080e−02	3.3826e−03	1.2741e−03	7.4851e−04

Accepted manuscript doi:
10.1680/jtran.23.00066

19-8-6-6-4	1.2885e−02	4.2034e−03	1.6100e−03	8.3753e−04
19-8-7-6-4	1.2151e−02	4.1813e−03	1.5587e−03	7.8088e−04

Table 4: The input values and range (used to generate the ANN training database based on the railway section near Leominster station, UK)

Railway track system	**Layers**	**Thickness (mm)**	**Poisson's ratio**	**Range of layer moduli (MPa)**
Five-layer system	Clean ballast (E_2)	300	0.2	70–170
	Contaminated ballast (E_3)	600	0.49	20–50
	Subgrade 1 (E_4)	2,100	0.49	50–100
	Subgrade 2 (E_5)	700	0.49	15–50
	Subgrade 3 (E_6)	6,100	0.49	100–400

Table 5: Details of geometries and moduli of the weakened zone for the ANN training database

	W_D (cm)	W_L (cm)	Y_w (cm)	E_w (MPa)
Weakened zone	0, 7.5, 10, 15, 20	0, 20, 40, 60	0, 15, 65, 125, 163.75	5%–50% E_4

Table 6: Details of case studies used for validation of the developed ANN-GA back-analysis technique

Case study No.	**Weakened zone angle (α)**	**Weakened zone expansion angle (θ)**	**weakened zone modulus (E_W)**	**weakened zone depth (W_D)**	**weakened zone length (W_L)**	**distance of the zone from the centre of the loading point (Y_W)**
1	Pipe crown (0°)	150°	25% E_4	7.5 cm	60 cm	15 cm
2	Pipe crown (0°)	150°	25% E_4	20 cm	60 cm	15 cm
3	Pipe crown	150°	35% E_4	7.5 cm	60 cm	15 cm

	(0°)					
4	Pipe crown (0°)	150°	35% E_4	20 cm	60 cm	15 cm
5	Pipe crown (0°)	150°	50% E_4	7.5 cm	60 cm	15 cm
6	Pipe crown (0°)	150°	50% E_4	20 cm	60 cm	15 cm

Table 7: Target and estimated values of the weakened zones in case studies 1 to 6

Parameter	Target value	Estimated value
	Case study 1	
W_D	7.5 (cm)	10 (cm)
W_L	60 (cm)	60 (cm)
Y_W	15 (cm)	15 (cm)
E_W	25.00% E_4 (17.96 MPa)	10.52 MPa (discrepancy= 41.51%)
	Case study 2	
W_D	20 (cm)	20 (cm)
W_L	60 (cm)	60 (cm)
Y_W	15 (cm)	15 (cm)
E_W	25.00% E_4 (17.96 MPa)	19.55 MPa (discrepancy= 8.90%)
	Case study 3	
W_D	7.5 (cm)	10 (cm)
W_L	60 (cm)	60 (cm)
Y_W	15 (cm)	163.75(cm)

E_W	35.00% E_4 (25.14 MPa)	21.38 MPa (discrepancy= 14.95%)
	Case study 4	
W_D	20 (cm)	20 (cm)
W_L	60 (cm)	60 (cm)
Y_W	15 (cm)	125 (cm)
E_W	35.00% E_4 (25.14 MPa)	27.07 MPa (discrepancy= 7.68%)
	Case study 5	
W_D	7.5 (cm)	10 (cm)
W_L	60 (cm)	20 (cm)
Y_W	15 (cm)	15 (cm)
E_W	50.00% E_4 (35.92 MPa)	30.69 MPa (discrepancy= 14.54%)
	Case study 6	
W_D	20 (cm)	20 (cm)
W_L	60 (cm)	60 (cm)
Y_W	15 (cm)	65 (cm)
E_W	50.00% E_4 (35.92 MPa)	37.8851 MPa (discrepancy= 5.49%)

Figure captions

Figure 1: Schematic of the methodology sequences

Figure 2: Schematic cross-section of the railway track substructure with a buried drainage pipe and soil weakened zone

Figure 3: The arrangement of geophones in a FWD test

Figure 4: Plan view of FWD test including loading points and geophone configuration for railway track application

Figure 5 (a-b): (a) A 3D FE model of the problem, (b) A close view of the loading point and locations of the geophones/data points

Figure 6 (a-b): (a) 2D and (b) 3D schematics geometry of the weakened zone in the FE model

Figure 7: Schematic illustration of the weakened zone at the pipe crown, showcasing variable θ

Figure 8: Effect of the expansion angle and position of the weakened zone around the pipe on the track surface deflection

Figure 9: RBF network (ANN surrogate forward model) structure

Figure 10(a-c): Accuracy of the ANN for estimating surface deflections at D_0

Figure 11(a-c)– Accuracy of the ANN for estimating surface deflections at D_{300}

Figure 12(a-c)– Accuracy of the ANN for estimating surface deflections at D_{1000}

Figure 13(a-c)– Accuracy of the ANN for estimating surface deflections at D_{1500}

Figure 14: Flowchart of the hybrid ANN–GA back-analysis technique

Figure 15: Results of the parametric analysis of the GA population and generation sizes

Figure 16: Effect of weakened size on weakened zone detectability using the back-analysis technique

Figure 17: Effect of Y_W on the RMSE and weakened zone detectability

Accepted manuscript doi:
10.1680/jtran.23.00066

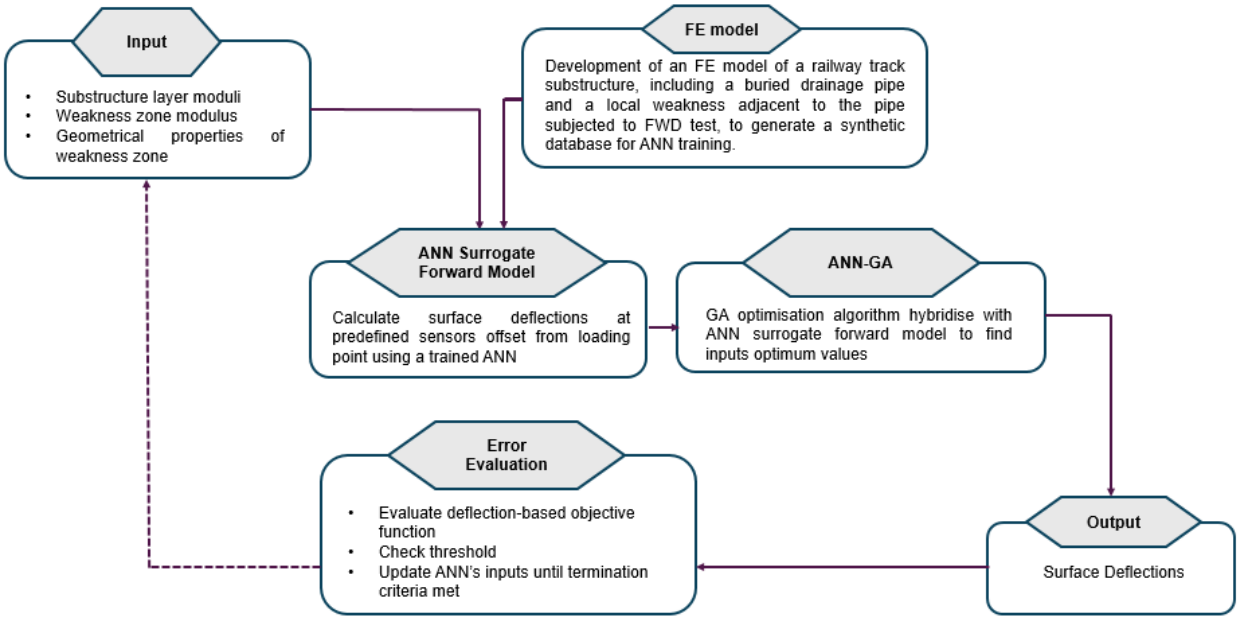

Fig. 1

Accepted manuscript doi:
10.1680/jtran.23.00066

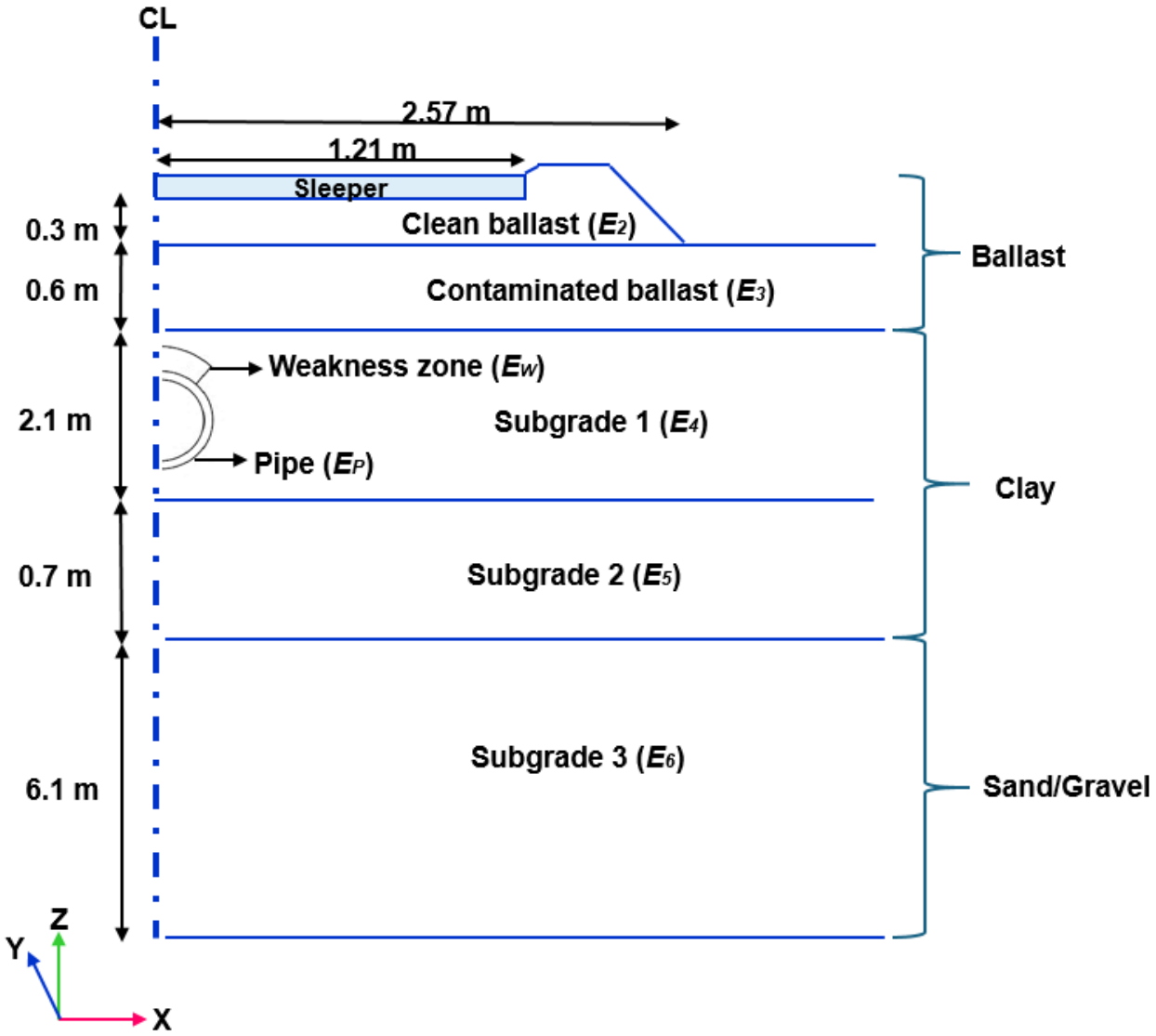

Fig. 2

Accepted manuscript doi:
10.1680/jtran.23.00066

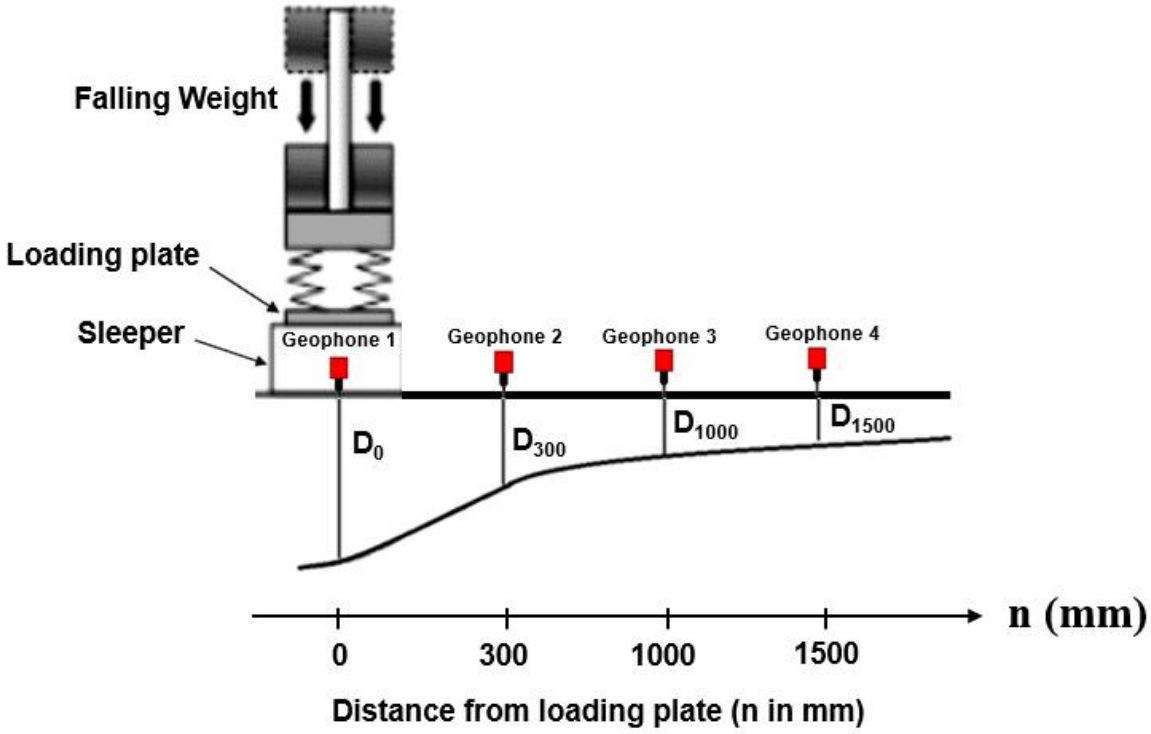

Fig. 3

Accepted manuscript doi:
10.1680/jtran.23.00066

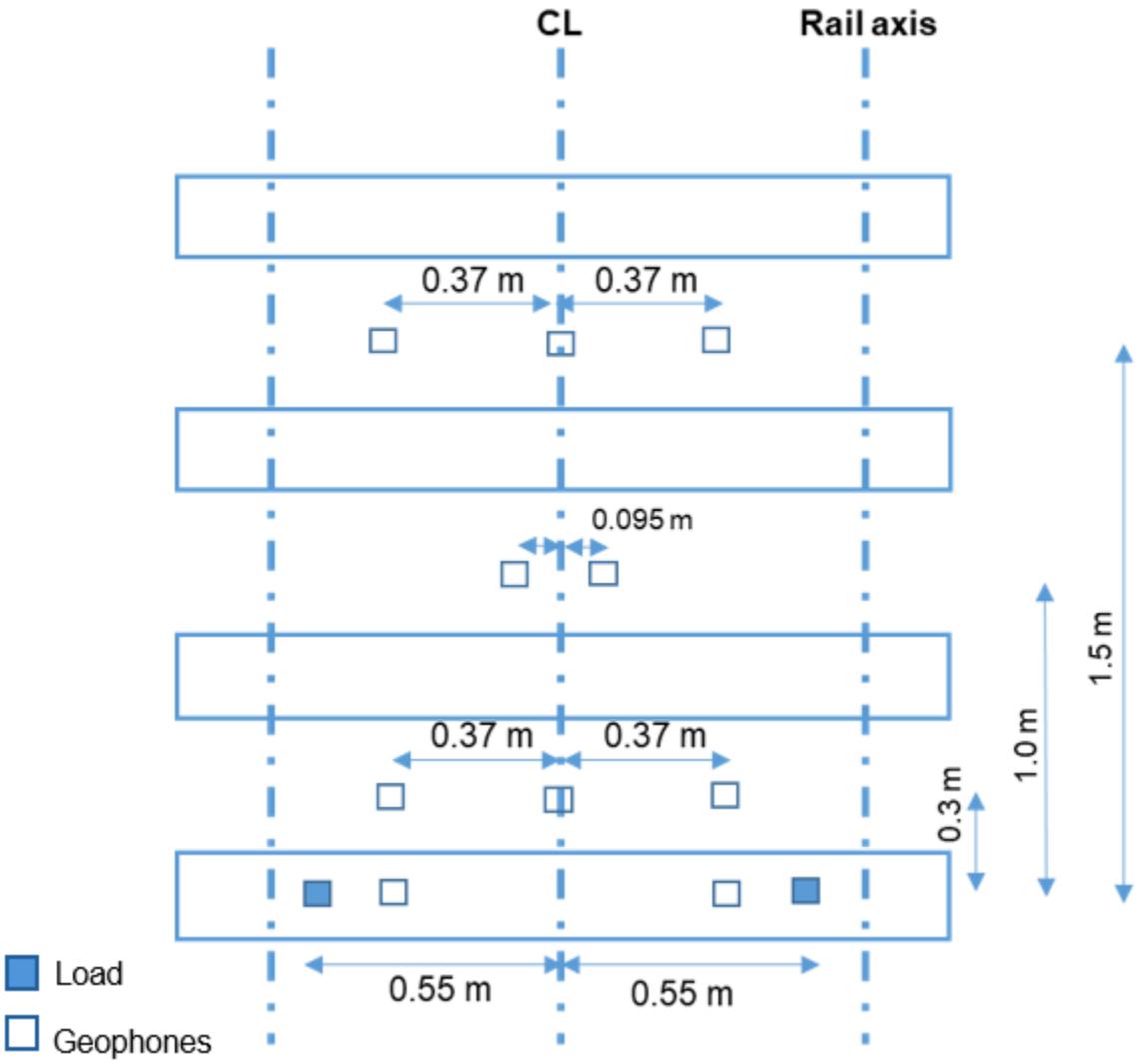

Fig. 4

Accepted manuscript doi:
10.1680/jtran.23.00066

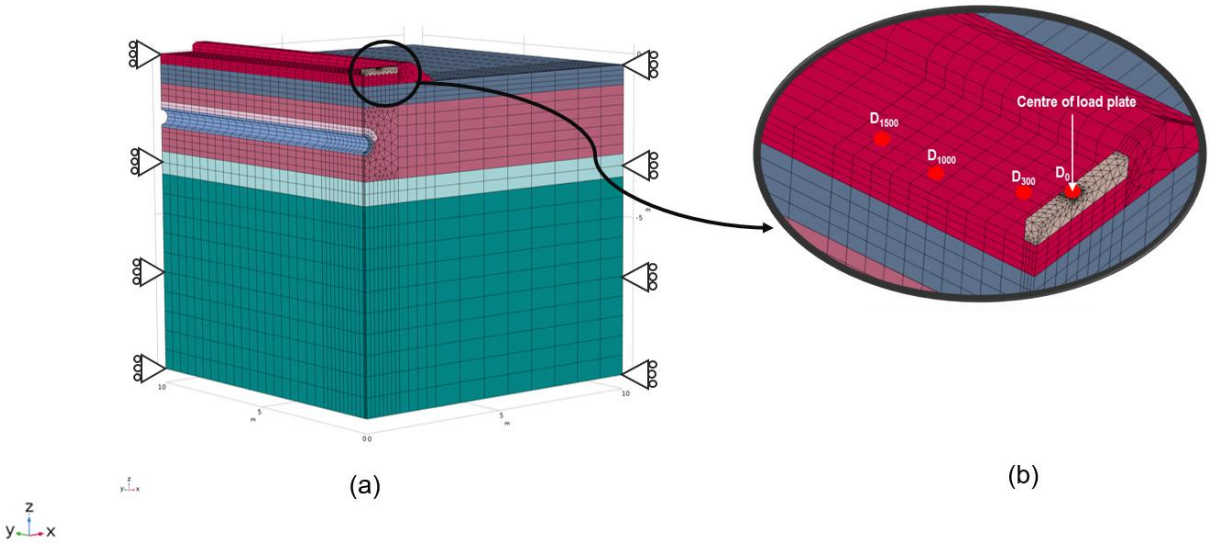

Fig. 5

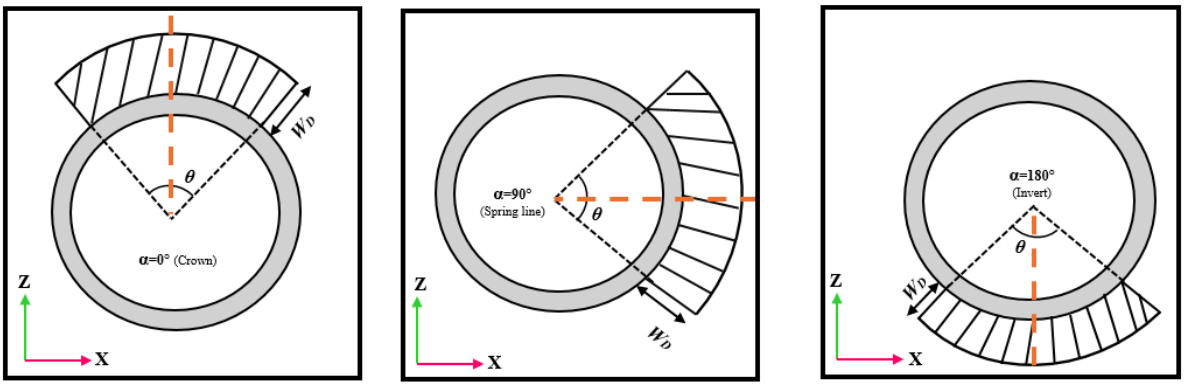

Fig. 6a

Accepted manuscript doi:
10.1680/jtran.23.00066

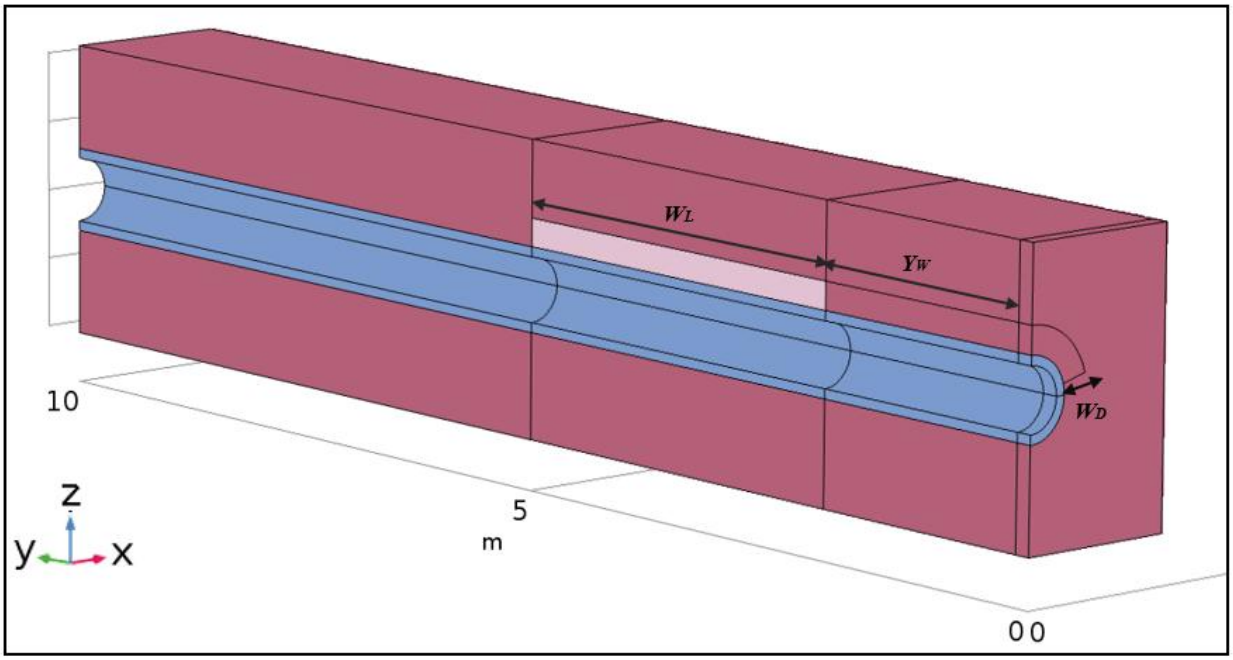

Fig. 6b

Accepted manuscript doi:
10.1680/jtran.23.00066

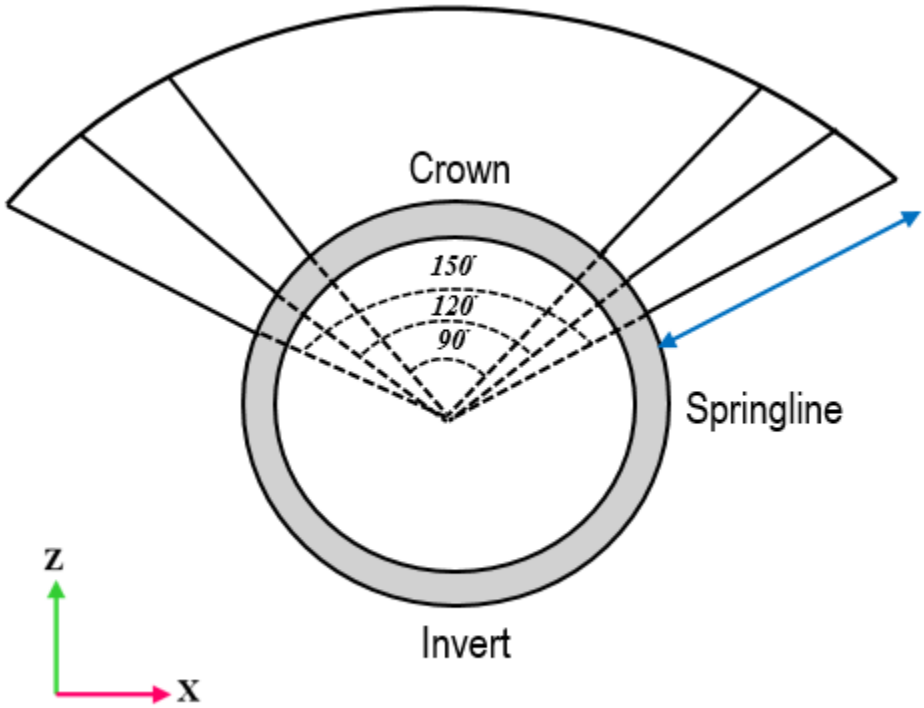

Fig. 7

Accepted manuscript doi:
10.1680/jtran.23.00066

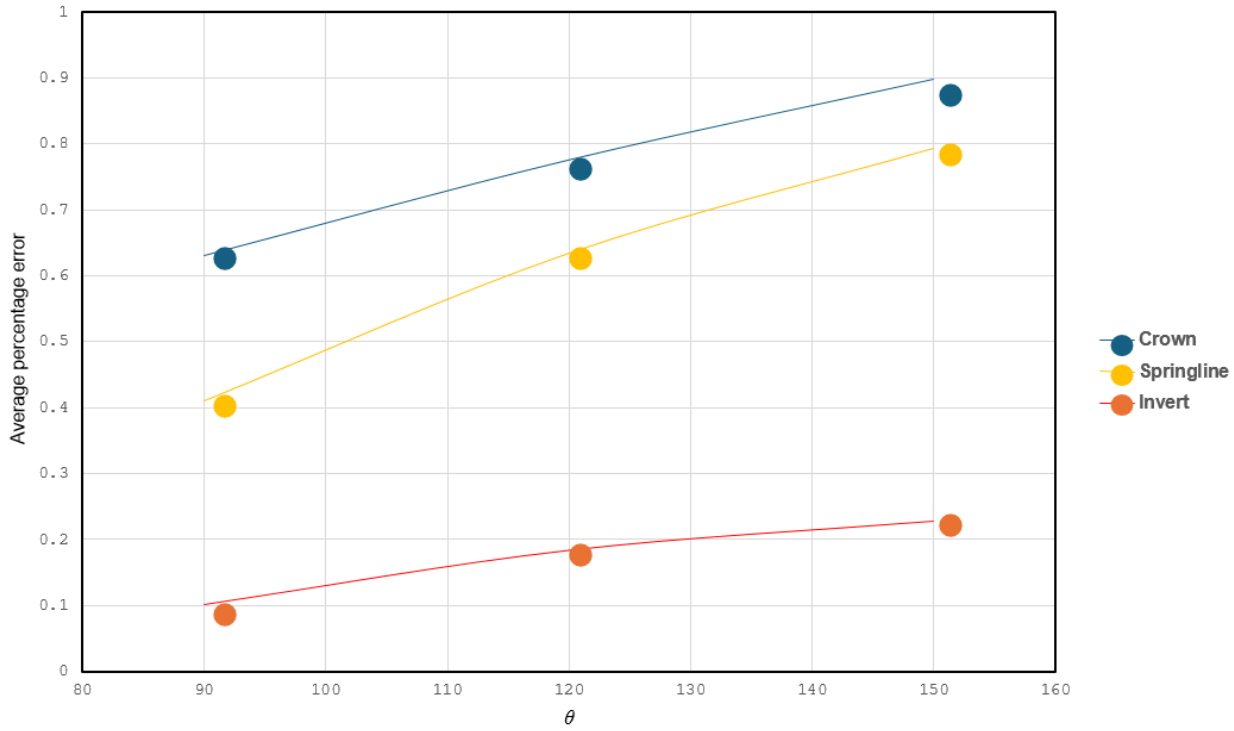

Fig. 8

Accepted manuscript doi:
10.1680/jtran.23.00066

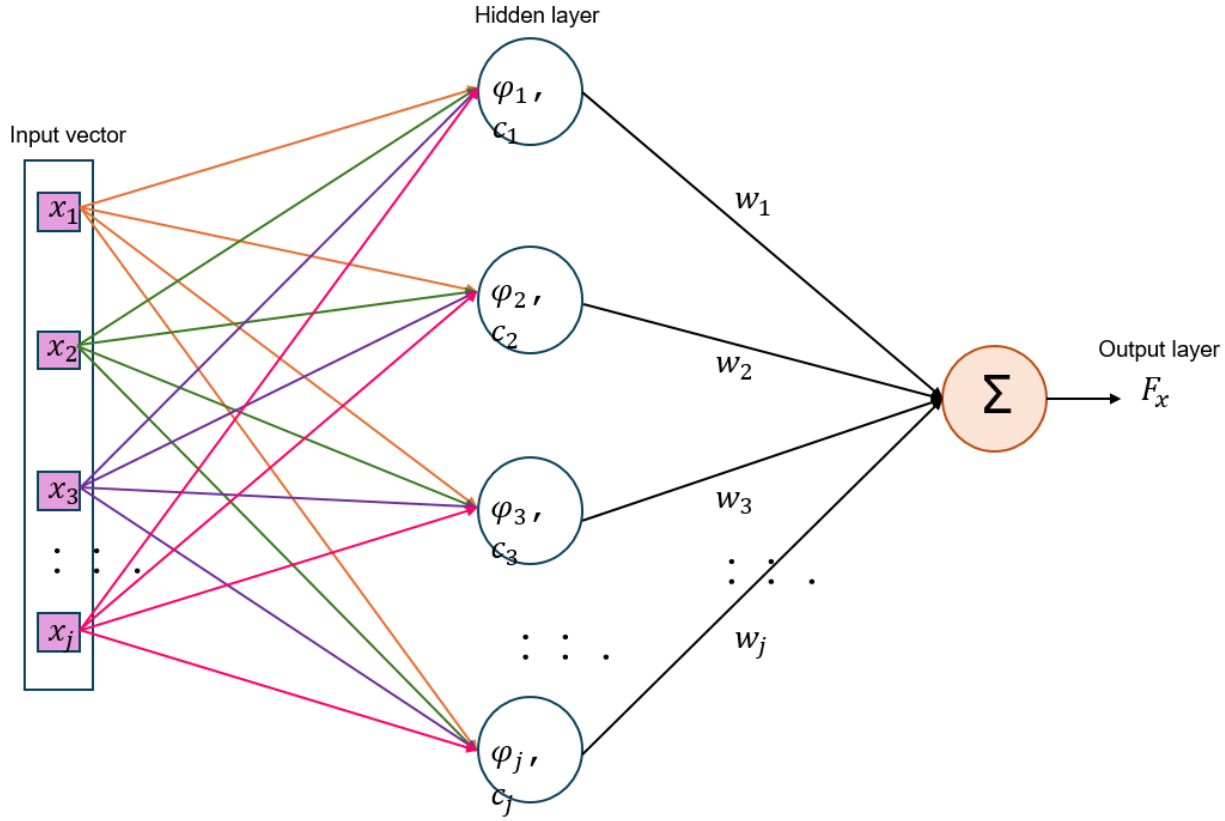

Fig. 9

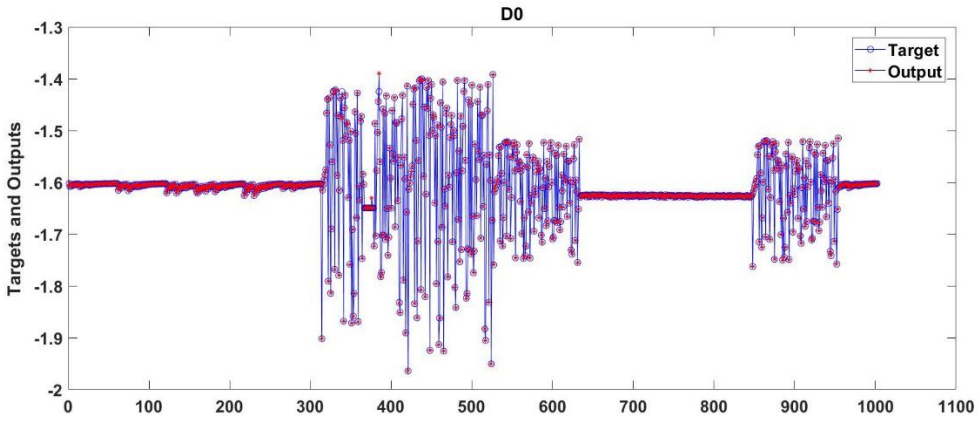

Fig. 10a

Accepted manuscript doi:
10.1680/jtran.23.00066

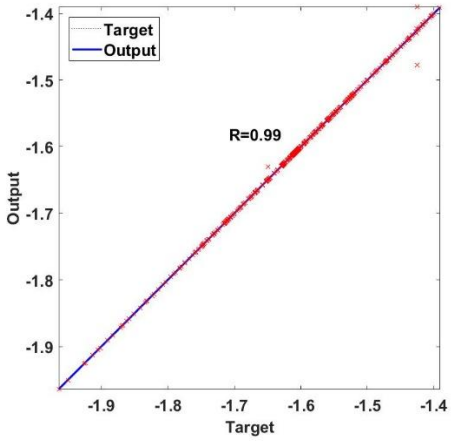

Fig. 10b

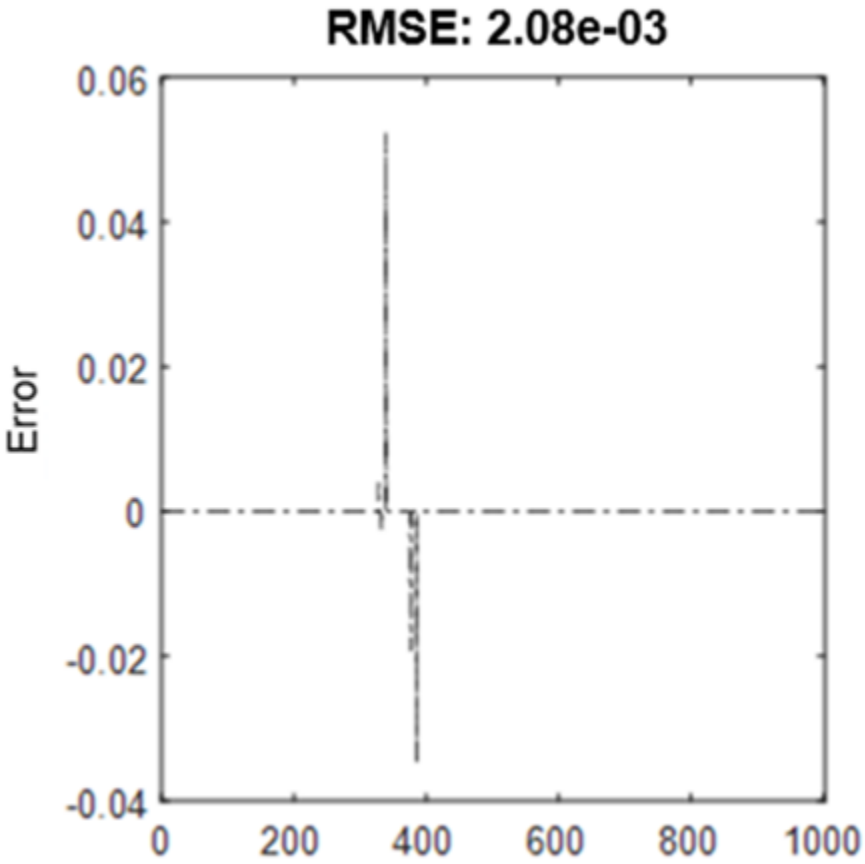

Fig. 10c

Accepted manuscript doi:
10.1680/jtran.23.00066

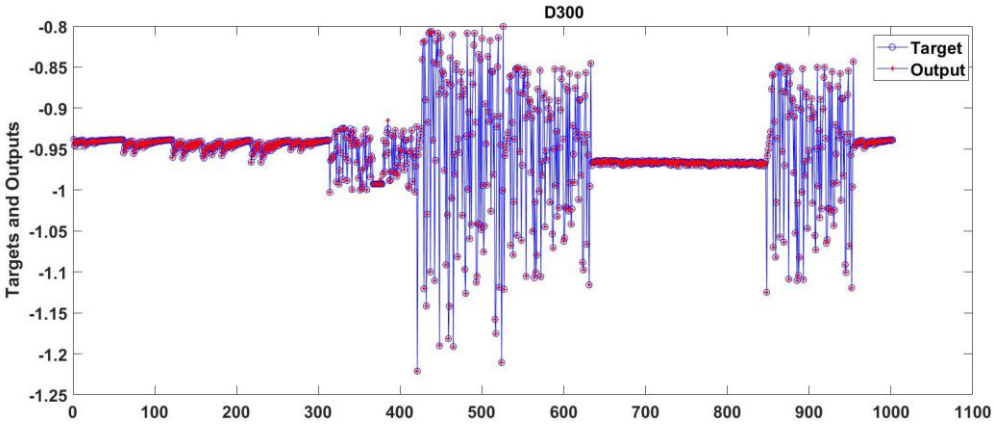

Fig. 11a

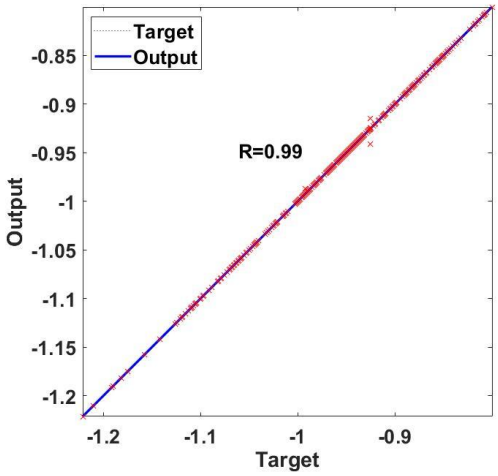

Fig. 11b

Accepted manuscript doi:
10.1680/jtran.23.00066

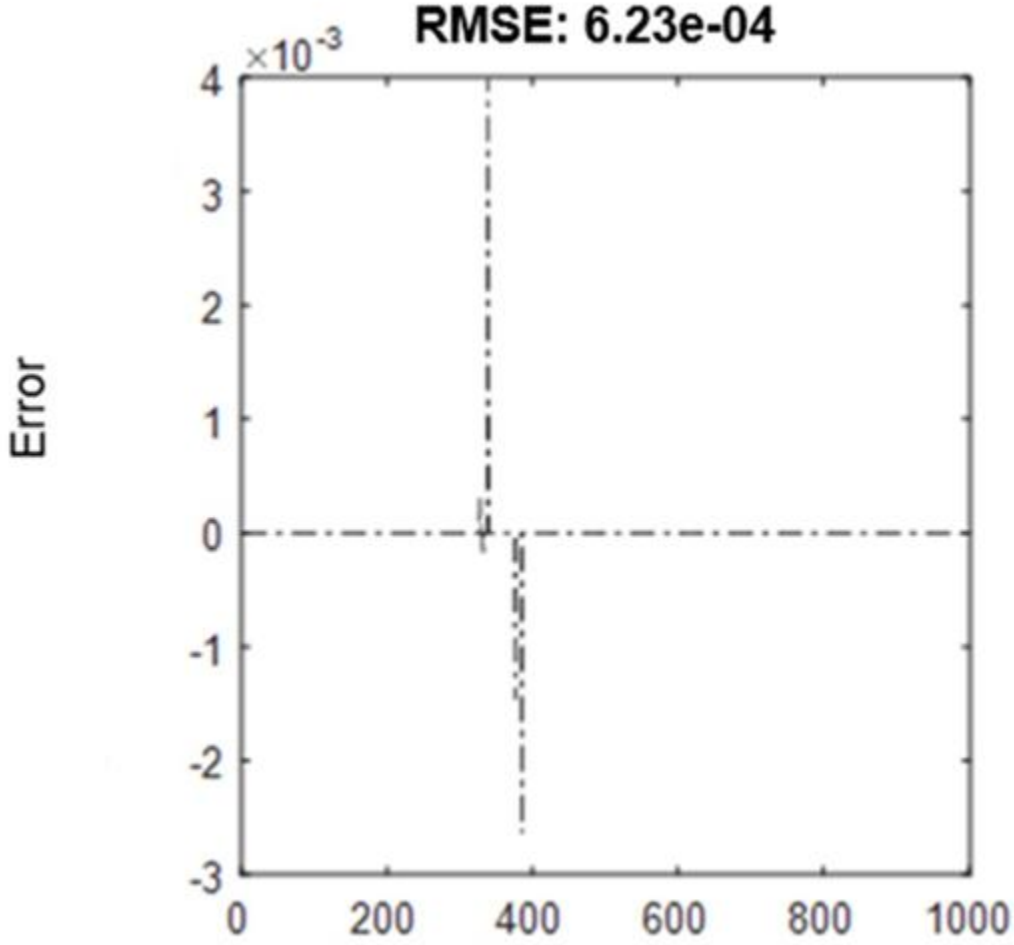

Fig. 11c

Accepted manuscript doi:
10.1680/jtran.23.00066

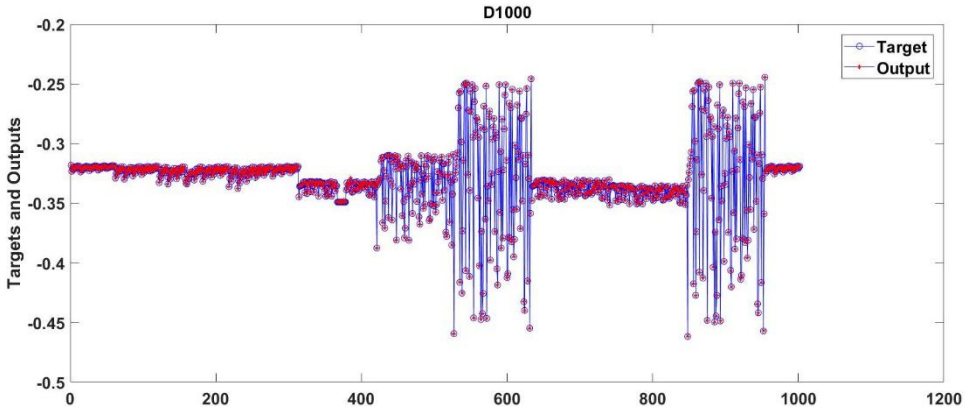

Fig. 12a

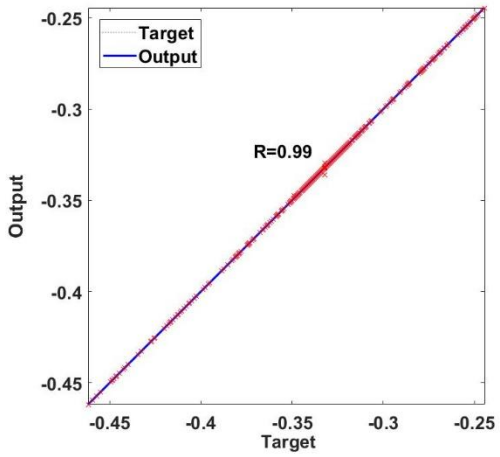

Fig. 12b

Accepted manuscript doi:
10.1680/jtran.23.00066

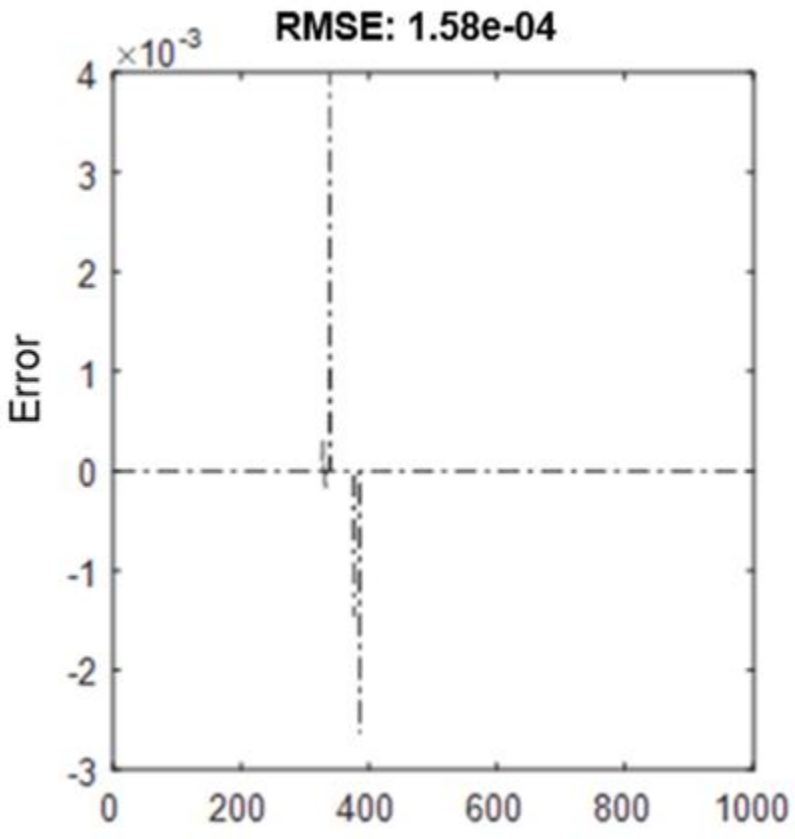

Fig. 12c

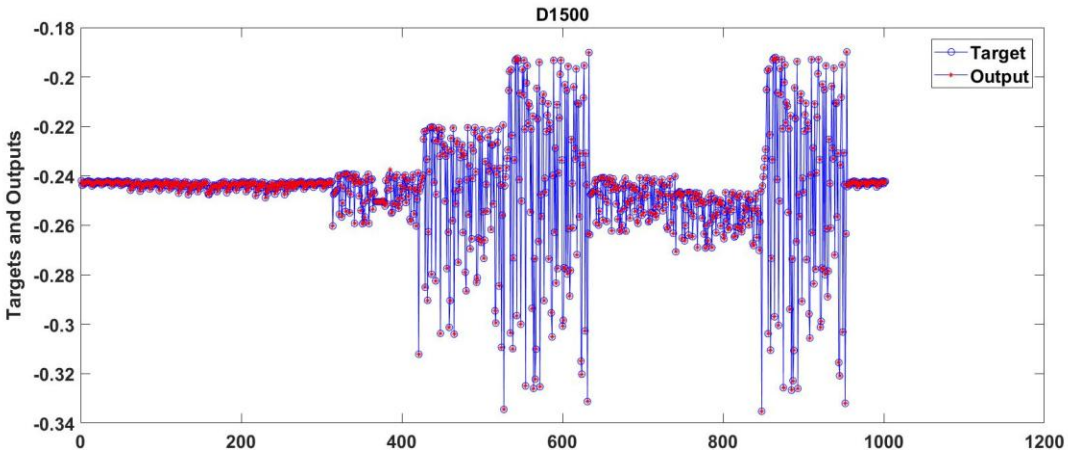

Fig. 13a

Accepted manuscript doi:
10.1680/jtran.23.00066

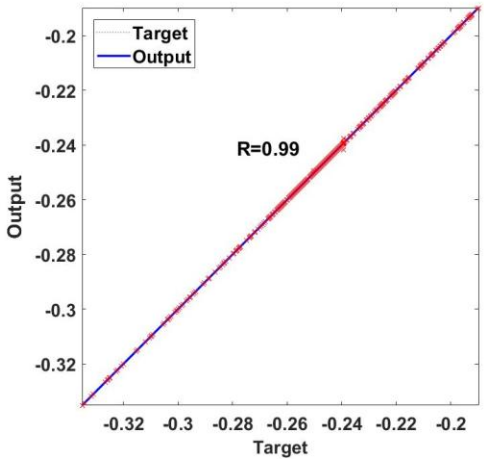

Fig. 13b

Accepted manuscript doi:
10.1680/jtran.23.00066

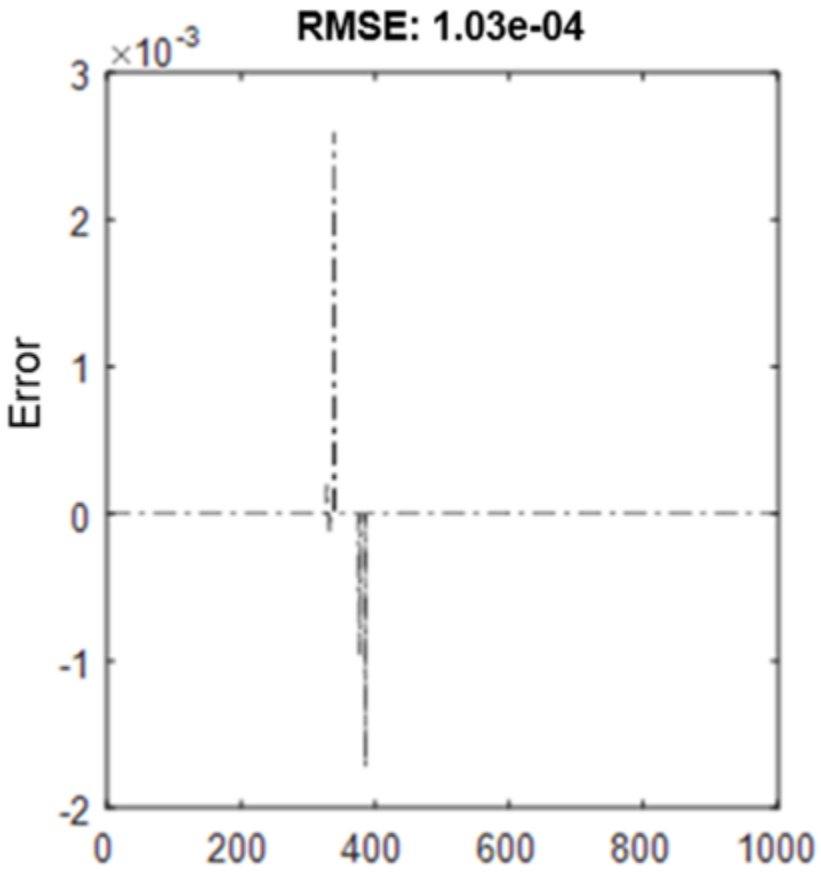

Fig. 13c

Accepted manuscript doi:
10.1680/jtran.23.00066

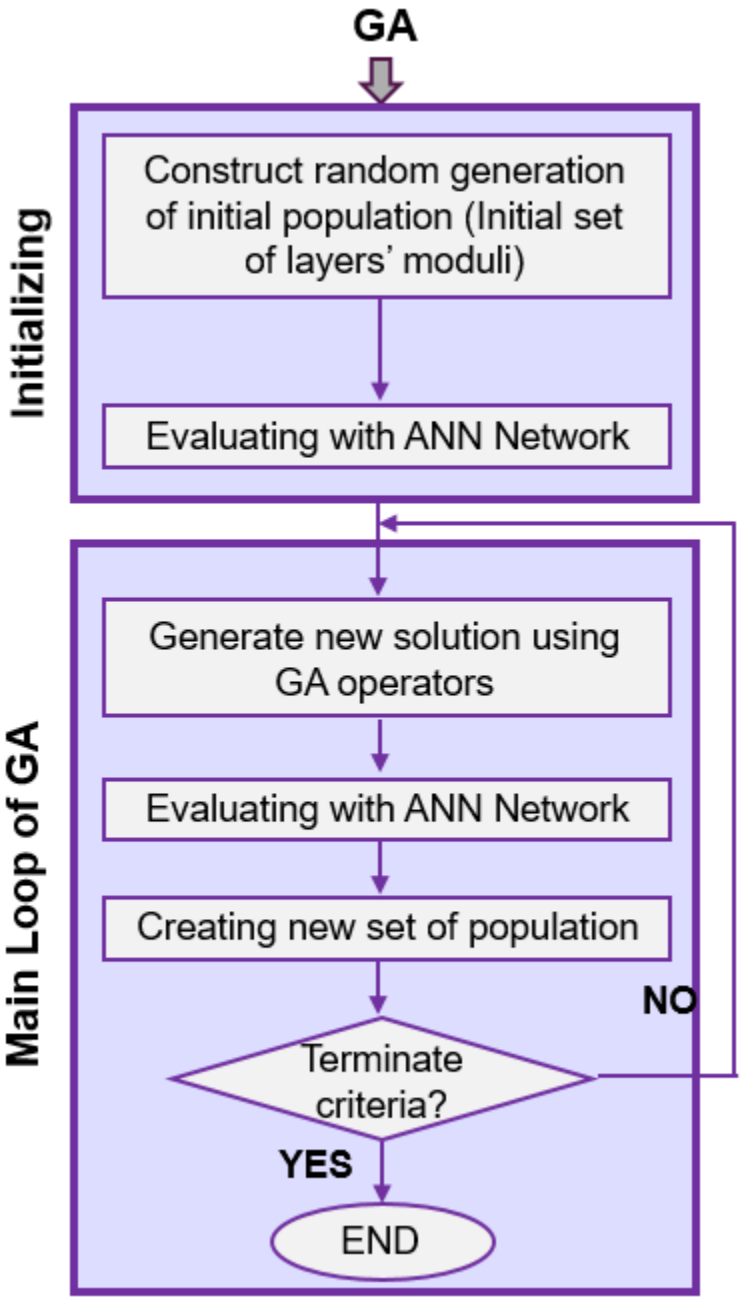

Fig. 14

Accepted manuscript doi:
10.1680/jtran.23.00066

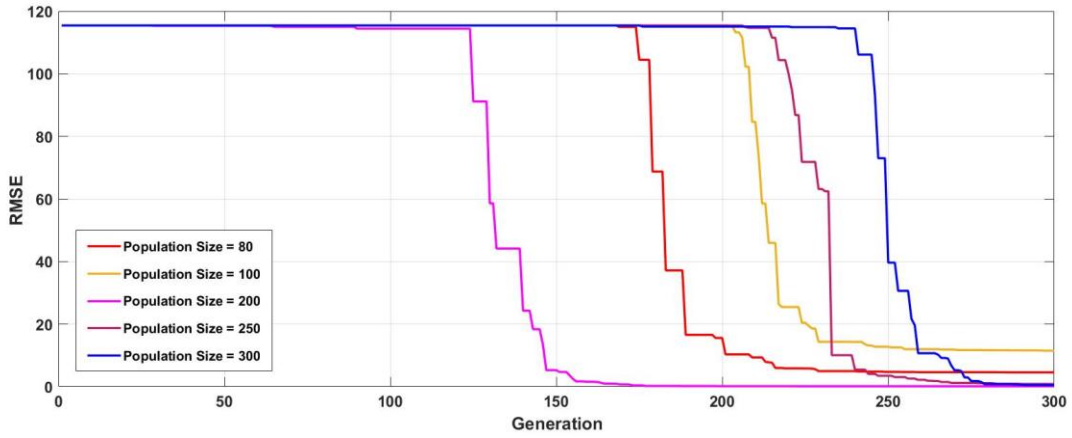

Fig. 15

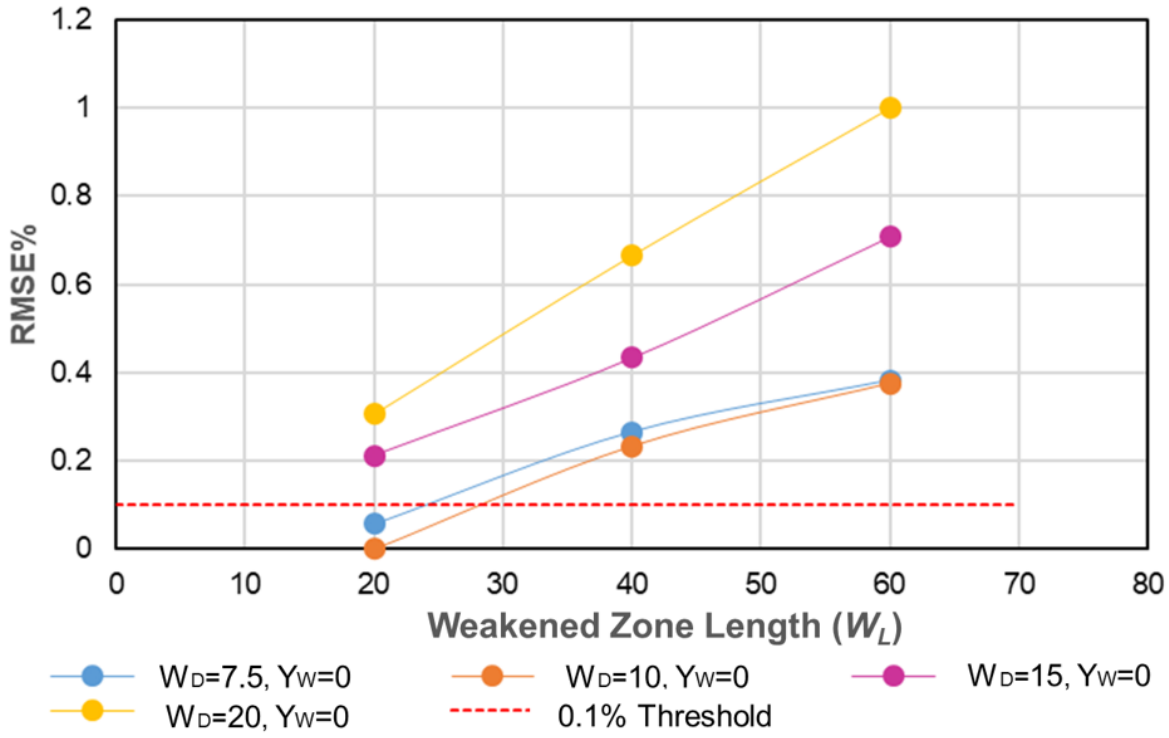

Fig. 16

Accepted manuscript doi:
10.1680/jtran.23.00066

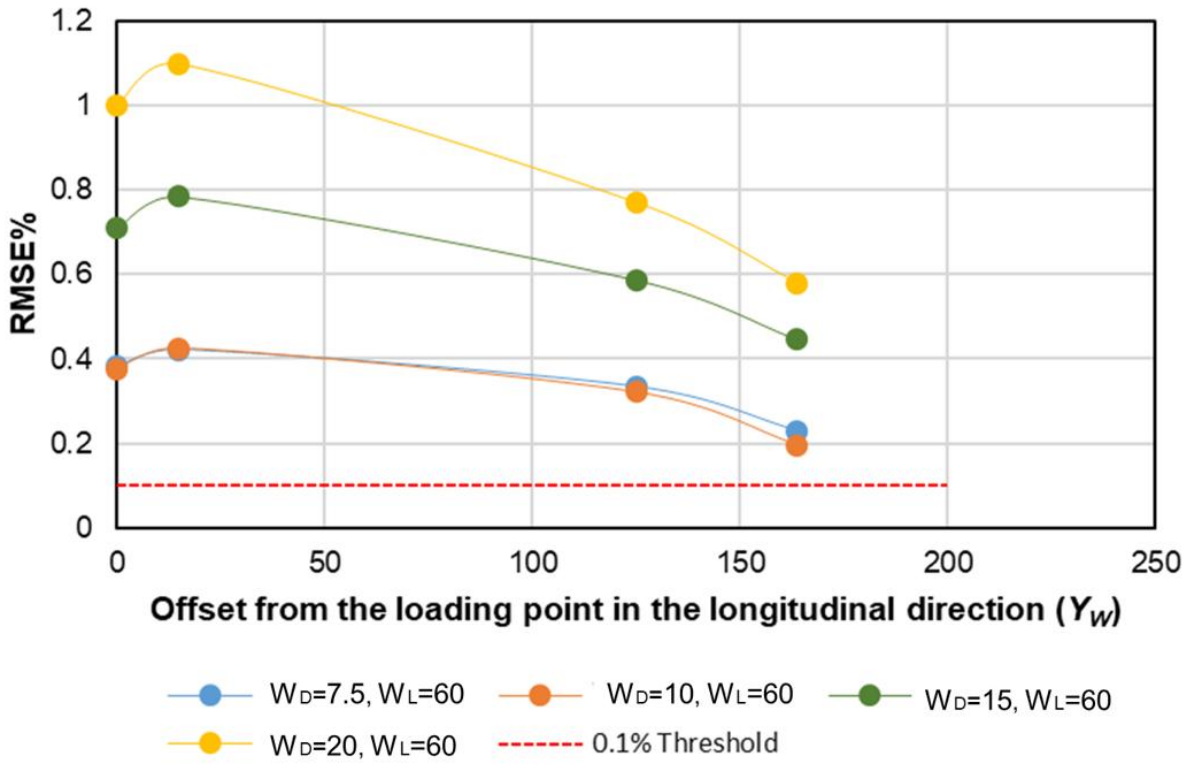

Fig. 17